ERDA

Progress Report

Radioisotope Studies Utilizing a Low Level Whole Body Counter

and

Clinical Applications of Activation Analysis.

April 30, 1976

Principal Investigator

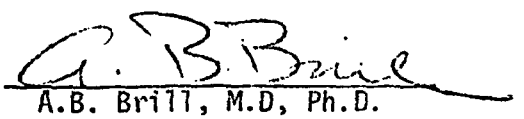

A.B. Brill, M.D, Ph.D.

Vanderbilt University
Medical Center
Nashville, Tn 37232

TABLE OF CONTENTS

A. Dosimetry and Tracer Kinetics
1. Methodology
a. Hardware Development

Progress on each of the proposed instrumentation projects is described in the following sections. Need for the development of these instrumentation systems grew out of our dosimetry projects. The whole body scanning bed was designed for mapping emission distributions (with the Anger Camera) and whole body transmission scans. The multienergy aperture camera interface permits the acquisition of data from 2 opposed cameras or for multiple tracers simultaneously. The newly arrived intrinsic germanium mosaic array will be used for mapping multiple tracers simultaneously in small animals for comparative dosimetry studies, as well as for high resolution patient studies. The CAMAC autonomous crate controller system development is designed to minimize data acquisition conflicts by more efficient utilization of computer systems. The probe-camera system provides data on blood clearance along with organ flow distributions for simulation, modelling, and dosimetry studies. Lastly, the video line buffer provides a monitor display of data being collected to verify the fact that systems are operating properly. A more detailed statement of the status of the particular projects follows.

1. Whole-body Scanning Bed

Figure 1 shows a block diagram of the scanning bed system as presently implemented.

Lack of space in our clinical facility caused a good deal of inconvenience when the scanning bed was introduced. The scanning bed requires a free floor space 14 feet by 5 feet in order to perform a whole body scan. At present all 3 of our scintillation cameras are located in a single room 16 feet by 37 feet and the routine commitment of the large amount of space required by the bed was unacceptable. Thus, until our new space (5000 square feet) is completed in January 1977, we are unable to use the scanning bed with the Anger Camera System.

In the light of such restrictions, we redirected the use of the bed for use with our new solid state detector array. The acquisition of the intrinsic germanium detector array (described section 3) required us to implement a means for moving the patients (since the detector had to remain stationary) for the purpose of evaluating the detector system in a laboratory remote from the clinic imaging area. This laboratory contains a PDP-11/10 with a Camac crate. Since the original interface and control system was designed and implemented using the CAMAC hardware available on the PDP-9 the moving of the scanning bed to the PDP-11/CAMAC system has been accomplished readily and as soon as the intrinsic germanium array holder is complete the system will be tested with the scanning bed.

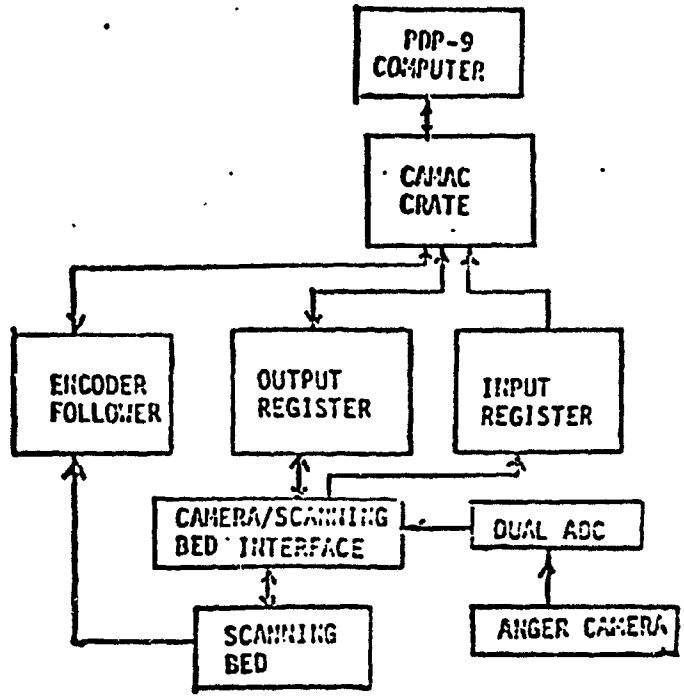

Figure 1 Block diagram of Scanning Bed Data Acquisition System.

2. Multi-energy Aperture Camera

Instead of a multienergy aperture camera interface, as originally conceived we have implemented a dual camera, dual isotope system. This can be extended to a more general system later, if the need arises.

The system, shown in figure 2, will provide us with the capability of performing dual isotope studies utilizing a single stationary scintillation camera operating in dual isotopes mode. When operating in dual isotope mode the scintillation camera uses two separate single channel analyzers to discriminate energy information and allows one to image 2 isotopic distributions simultaneously. Information from the camera operating in this mode is transmitted to the computer interface on a set of 4 wires. The same pair of cables carry X, Y position information for both energies but a separate Z cable is used for each. The dual ADC accepts these four signals and provides an indicator bit in the digital data to indicate in which energy window the interaction occurred.

In order to do quantitative measurements with the Anger camera we needed to collect data from opposed cameras simultaneously. Thus, as an extension of this dual isotope capability we designed and constructed a scintillation camera multiplexer shown in the block diagram of Figure 3. In effect, this multiplexer causes two separate cameras operating in single isotope mode to appear to the dual isotope interface as a single scintillation camera operating in dual isotope mode.

The multiplexer uses two high speed analog swtiches to transmit

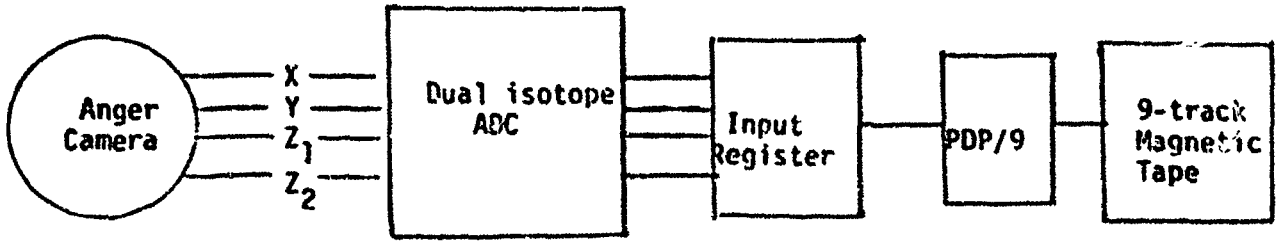

Figure 2. Dual Isotope Data Collection System.

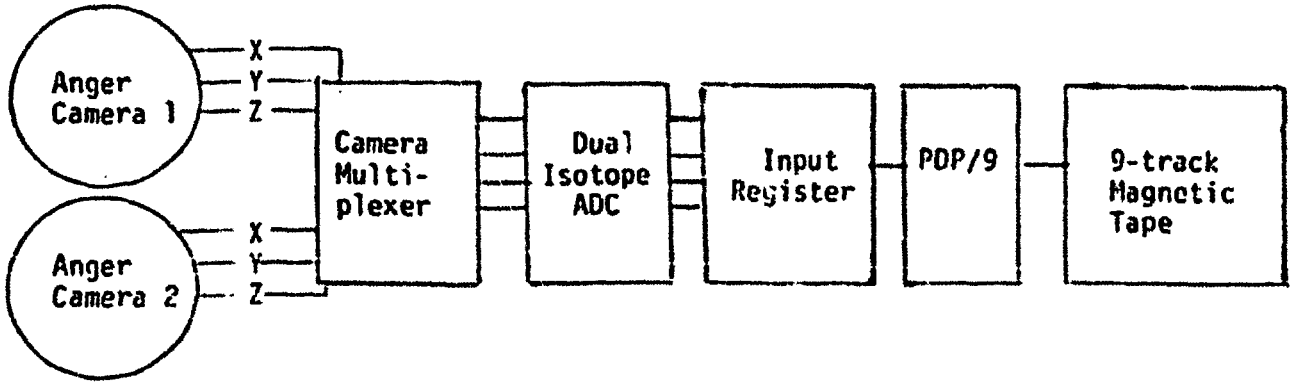

Figure 3. Block diagram of dual camera data collection system using a scintillation camera multiplexer to simulate a dual isotope input.

the X, Y position signals from the appropriate camera to the dual isotope ADC upon receipt of a Z pulse from the camera. The multiplexer is then locked in this state until the ADC indicates that it has completed the conversion. When used the multiplexer causes no interaction between the cameras because the analog switches are designed to disconnect one before connecting the other. The other concern in this system is the loss of counts due to the dead time of the system. If one considers the multiplexed cameras as a simple anti-coincidence system the loss due to coincidence (C_L) can be calculated by the standard coincidence equation:

$$C_L = 2\, C_1\, C_2\, \tau$$

where C_1 = count rate of camera 1

C_2 = count rate of camera 2

τ = dead time of the multiplexer

If $C_1 = C_2 = 5000$ cps and $\tau = 10$ µs

the loss is only 500 cts/sec or 10%.

The multiplexer is so designed that a high count rate in one camera will not cause an inordinate loss of counts in the other camera image. At high count rates the multiplexer will simply toggle between the cameras.

The dual camera multiplexer has been completed and will allow us to use the dual isotope computer collection system to do clinical dosimetry studies for regions that are located between the opposed detectors. One study for which we designed the system is Xe-133 lung ventilation in which a patient inhales the Xe-133 gas while positioned between two scintillation cameras. The images obtained in this situation indicate which areas of the lung are being properly ventilated, and due to the low energy of Xe-133, and geometrical considerations, a dual camera system is of great utility for clinical and dosimetry studies. Applications for renal studies are also proposed.

An important justification for the dual camera system is the use of geometric mean calculations to increase the accuracy of isotopic flow and dosimetry studies by using two opposed scintillation cameras.

We are currently writing software which will allow the use of the dual isotope/dual camera data acquisition system. Because of the identical formats of the data one set of software is being written and will be used whether the data collected are from dual isotope or dual camera configurations. We are awaiting a level converter/line driver circuit to be delivered by Ohio Nuclear for a new portable scintillation camera we have just received which will be one of the elements in the dual camera system. The portable camera is required for the dual camera system because it is not possible to place opposed detector heads of our Nuclear Chicago stationary cameras close enough together to be useful for this purpose.

3. Intrinsic Germanium Detector Array

The use of solid state or semiconductor detectors makes it possible to very accurately map isotope distributions and permits the simultaneous mapping of multiple isotope distributions. These two characteristics of semiconductor detectors make them very attractive for use in determining internal dosimetry data from radioisotopes. However, sensitivity due to their small size has always limited the usefulness of these detectors. To solve this problem, Goulding and Pehl at the Lawrence Berkeley Radiation Laboratory designed and fabricated a mosaic detector system under funding by a one year grant from NIH (April 1974-1975). This system arrived at Vanderbilt in November 1975 and preliminary evaluations and monitoring of the system have been performed.

The intrinsic or high purity (HP) germanium (Ge) detector array shown in Figure 1 consists of 9 detectors each 35mm in diameter, 1 cm thick, arranged in a 3 x 3 matrix with 50mm between centers. The 9 detectors are cooled by a common liquid nitrogen reservoir. The electronics associated with the system (Figure 2) include two single channel analyzers (SCA) for each detector coupled to the linear amplifiers. All nine detectors are powered by a common high voltage supply with a voltage divider network employed to maintain each detector at its optimum operating voltage. One of our primary concerns with this system was the stability and lifetime of multiple detectors in a common cryostat. We have now monitored the system for six months and curves of leakage current vs. time for each of the detectors are shown in Figure 3. Eight of the nine detectors have remained very uniform in performance with fluctuations seen only when the high voltage was reduced to make alterations of the operating configuration. However, detector #7 began to show an excess in current leakage shortly after arrival. It has now been disconnected from the system high voltage supply and placed on a separate supply so that high voltage can be applied only when the system is to be used. This problem is believed to be due to a small amount of contaminant on the surface of the detector and probably can be removed by recycling the vacuum of the system. This will be attempted after preliminary studies with the system are concluded.

Energy resolution and relative sensitivity measurements made with a point source of Tc-99m at 3 feet from the front surface of the detectors are shown in Figure 4. These data show that the detectors and electronics are very closely matched and the resolution is excellent.

For routine frontal plane scanning 19 hole focussed collimators with a geometric resolution of 0.22 inches and a focal length of 3.25 inches have been designed and constructed. Line spread functions for these collimators measured with a Tc-99m (140keV) line source in air are shown in Figure 5. These collimators have excellent resolution and relatively uniform response from 1 to 5 inches from the face of the collimator.

The detector electronics have been interfaced to a PDP/11 minicomputer via CAMAC for data acquisition. The system is designed to remain stationary during an imaging procedure with the object to

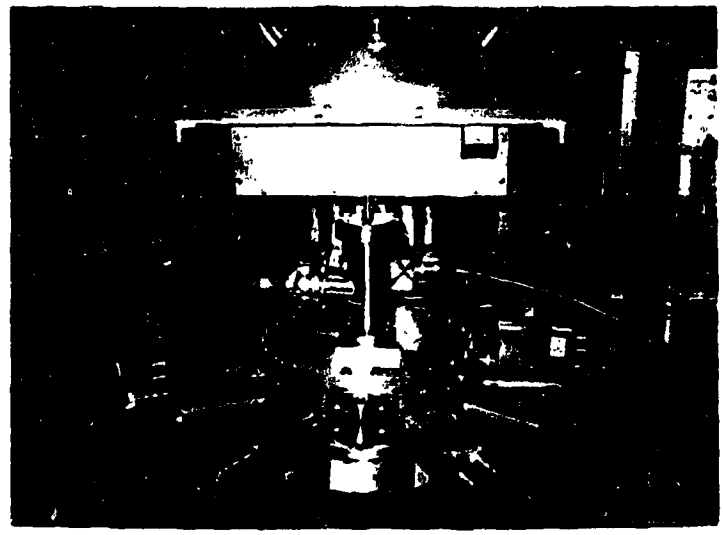

Fig. 1 Photograph of nine detector intrinsic germanium system.

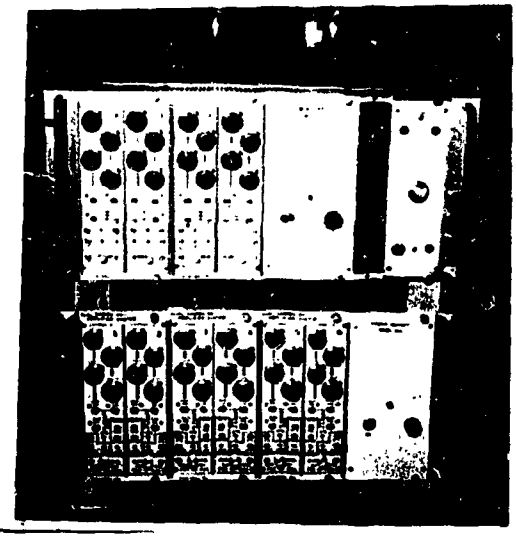

Fig. 2 Photograph of electronics for the intrinsic germanium detector system.

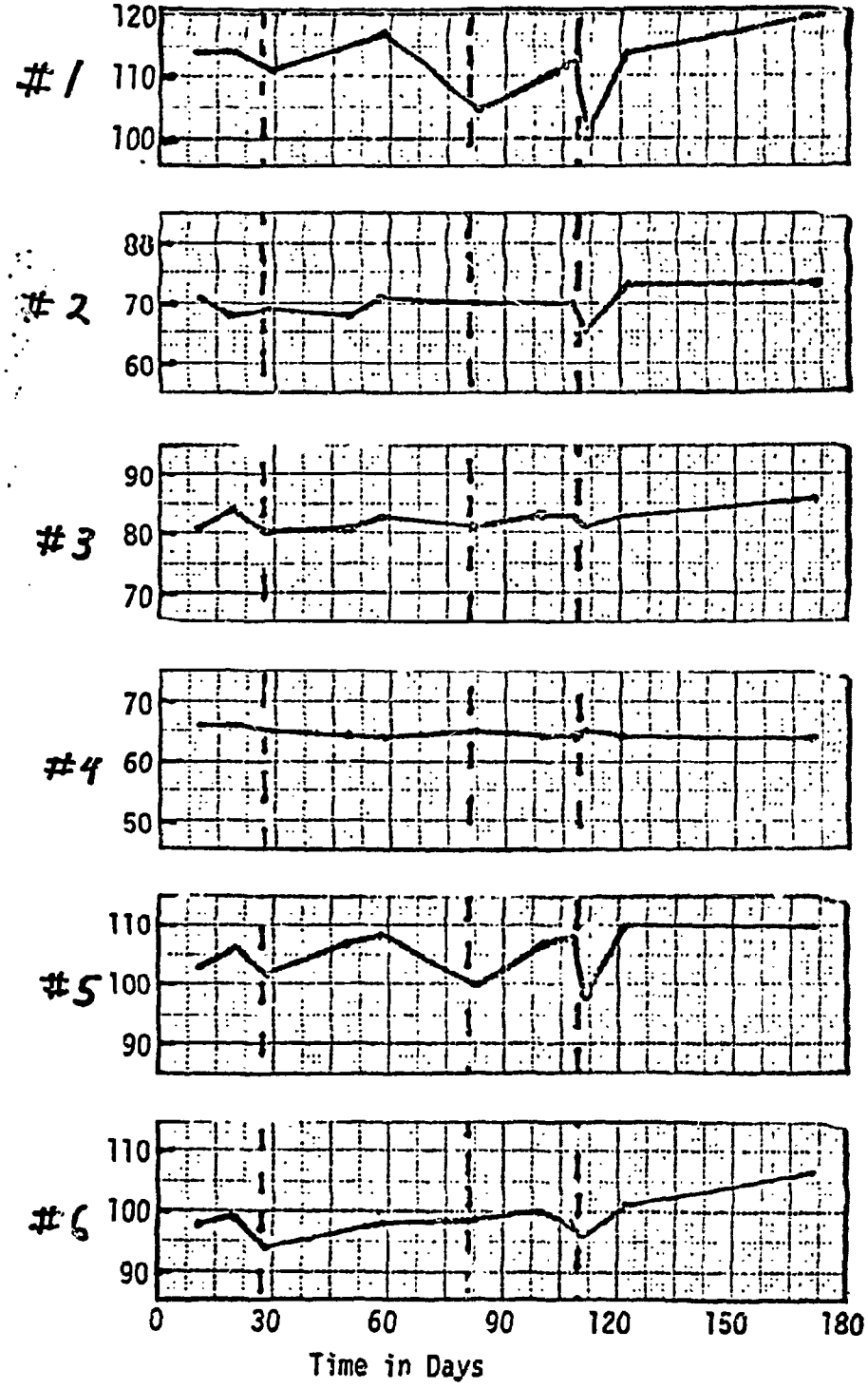

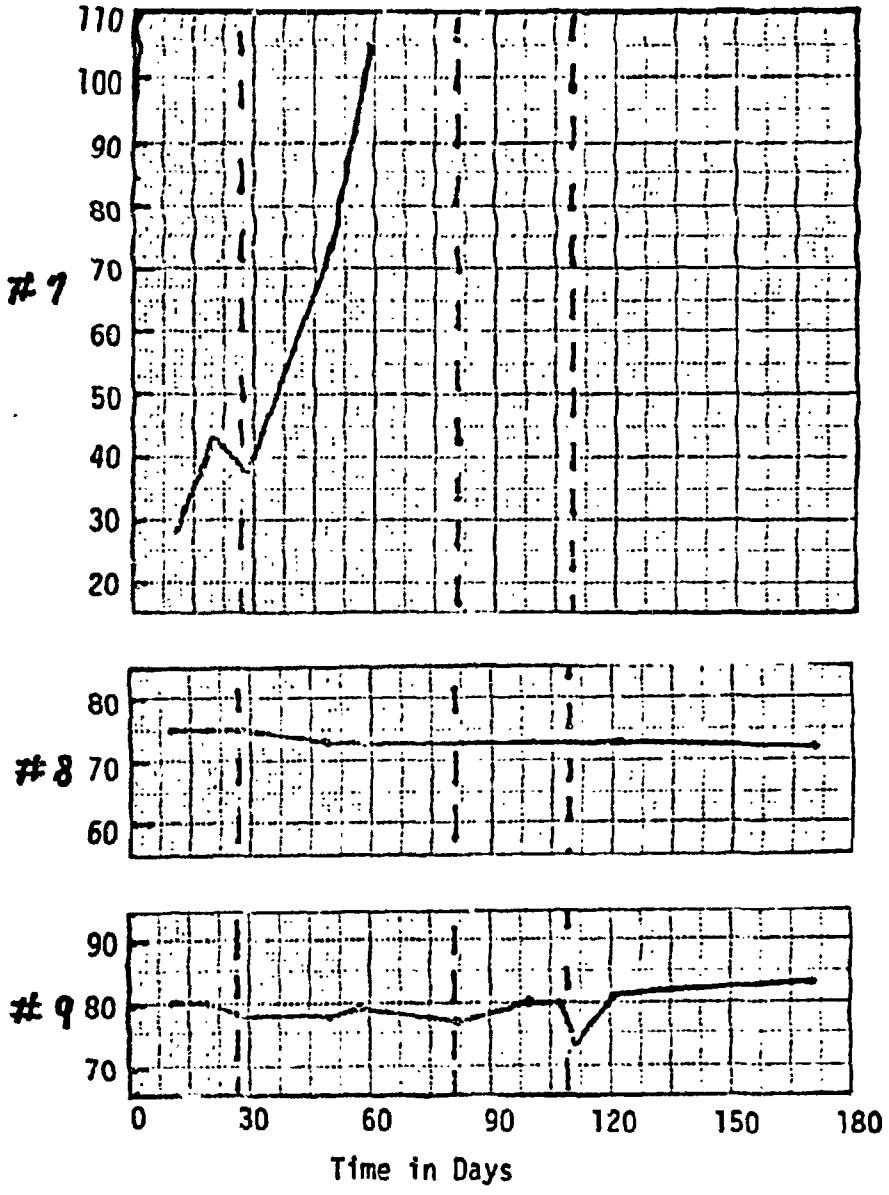

Fig. 3 Leakage Current measurements vs. time for each of the 9 detectors in the intrinsic germanium detector array. The units of the Y-axis are in millivolts and are directly proportional to the actual current values. The dashed lines indicate times the detectors were powered down.

DETECTOR	ENERGY RESOLUTION (keV)	% RESOLUTION	UNCOLLIMATED RELATIVE SENSITIVITY (%)	COLLIMATED RELATIVE SENSITIVITY (%)
1	1.13	0.81	110	114
2	1.13	0.81	108	91
3	1.17	0.84	98	87
4	1.18	0.84	114	118
5	1.11	0.79	100	94
6	1.12	0.80	78	90
7	1.06	0.76	102	99
8	1.06	0.76	94	102
9	1.14	0.81	95	105

Fig. 4 Energy resolution and uncollimated relative sensitivity measurements were made with a Tc-99m point source at 3 feet from the surface of the detectors. Collimated sensitivity measurements were made with a plane source of Tc-99m .

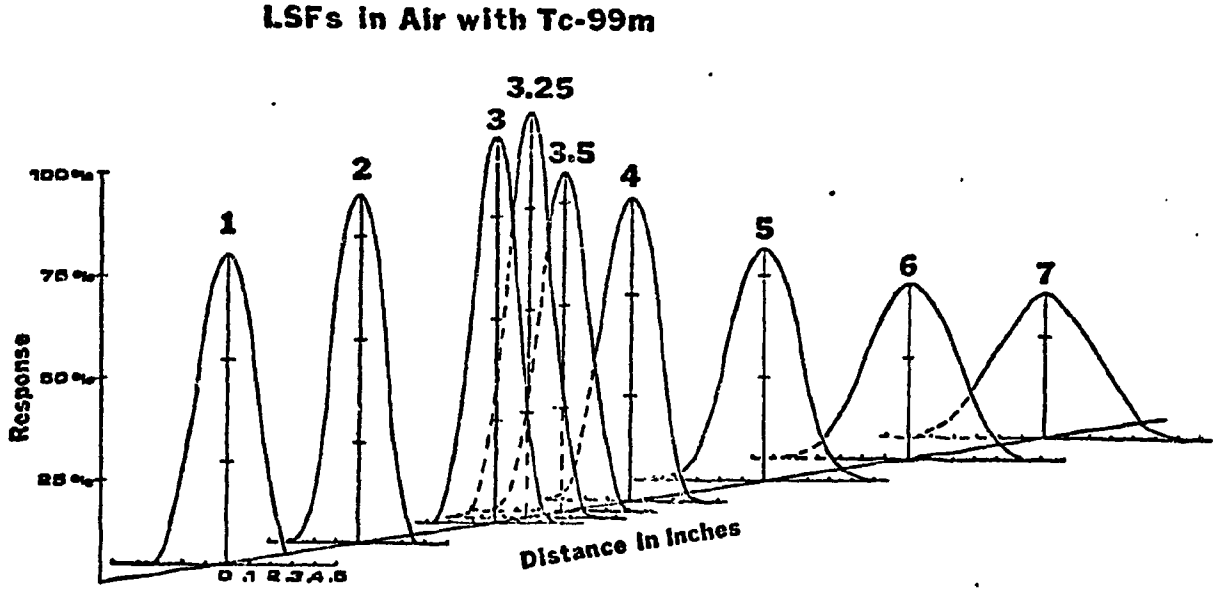

Fig. 5 Line spread functions of the 19 hole focussed collimators constructed for use with the intrinsic germanium detectors.

to be imaged being moved in an x-y raster. Two modes of operation are available with the instrument.

For phantom and small animal studies the collimated system is suspended over a precision stepping motor-controlled x-y drive system. This scanning system is also interfaced to the PDP/11 computer via CAMAC as shown in the block diagram in Figure 6. The x-y scanner is moved in a rectilinear raster under computer control and data are collected from each of the 18 single channel analyzers (2 for each detector, i.e. 2 photopeaks) simultaneously. Interpretive language programs have been written such that by moving the object to be scanned in a 50 x 50mm raster (50mm is the distance between detector centers) and collecting 21 x 21 (medium spatial resolution (2.4mm/point)) or 42 x 42 (high resolution (1.2mm/point)) data points from each detector a 64 x 64 or 128 x 128 array can be constructed corresponding to a 150 x 150 mm scan field. The detectors and electronics are very closely matched in efficiency and performance making it possible to normalize between detectors by counting a plane source of activity with each detector and thereby obtaining correction factors. A 64 x 64 data point scan of a 125 x 125 mm line phantom of Tc-99m is shown in Figure 7 to demonstrate this data collection technique.

For large animals and patients the computer is interfaced to our scanning bed (dashed lines in Figure 6) which can be moved in an x-y raster under computer control. This interfacing was accomplished initially on our PDP/9 computer via CAMAC (see section A.1a1) and the same system is being duplicated for use with the PDP/11. The system will operate in the same fashion as for the stepping motor-controlled system described above. In scanning areas larger than 150 x 150 mm, the scanning bed is being programmed such that multiple scan fields will be mapped and the resulting data will be rearranged in the computer to produce a single image corresponding to the total scan field. A C-frame support arrangement has been designed and constructed (Figure 8) so that the detector array will be suspended over the scanning bed with the only possible movement being in the vertical direction for positioning. The detector system will then be self-contained with the electronics mounted at the back of the C-frame.

The system as currently used has the ability of selecting two energy windows per detector. However, it may become necessary to select a large number of windows and this may be accomplished by use of an ADC and signal routing information derived from a relatively wide window SCA. A diagram showing the ADC system to be used with 9 detectors is shown in Fgiure 9A. The dotted lines indicate additional electronics that we borrowed to test the system concept. A wide window is set to include the region of the spectrum to be analyzed by each detector. This is a routing and gating pulse to start digitization in the ADC. Analog inverters are needed between the linear amplifiers and the ADC inputs because the germanium electronics produce positive signals while the CAMAC ADCs require negative inputs. Timing required by the ADCs is such that the gate signal must bracket in time the analog signal to be digitized. The system would function in the following manner. When an event is detected by one of the detectors and falls into the region of the spectrum to be analyzed, a gate pulse is sent to the ADC to start digitization. After 12.5 micro-seconds an 8 bit digitized value is available for reading by

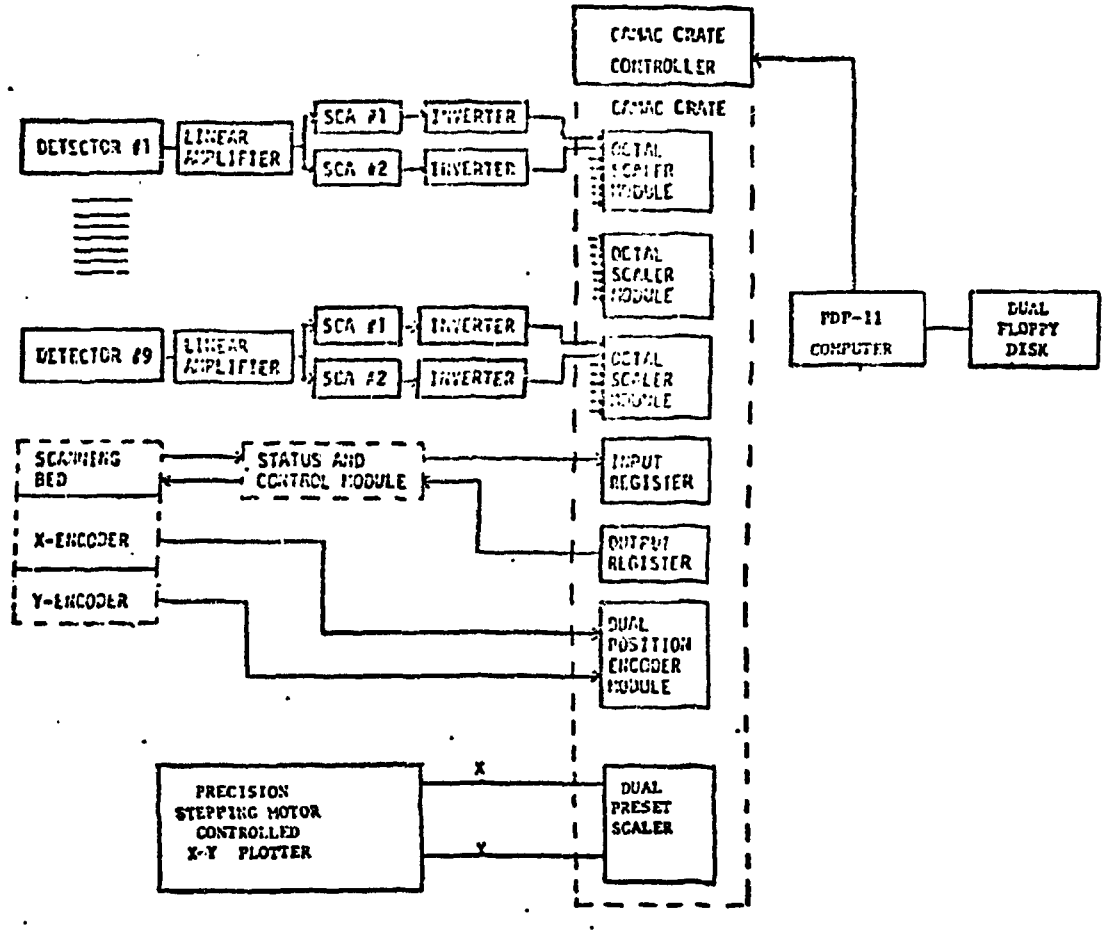

Fig. 6 Block diagram of data acquisition system for intrinsic germanium detector array.

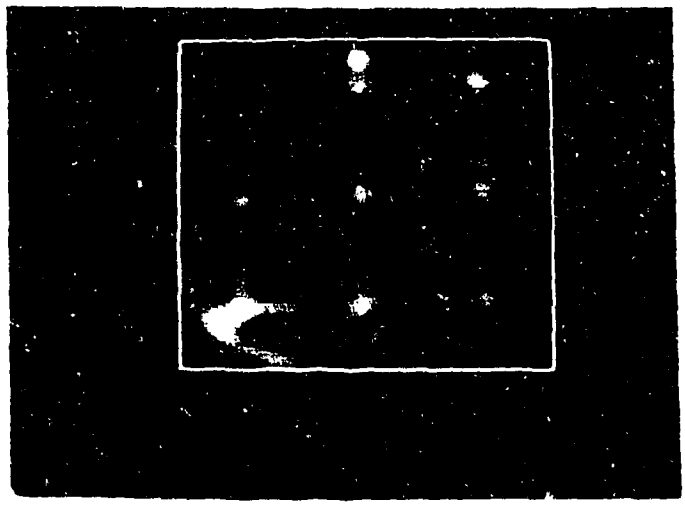

Fig. 7 Photograph of scan of line phantom imaged with intrinsic germanium system. White frame corresponds to a 150 x 150 mm. area.

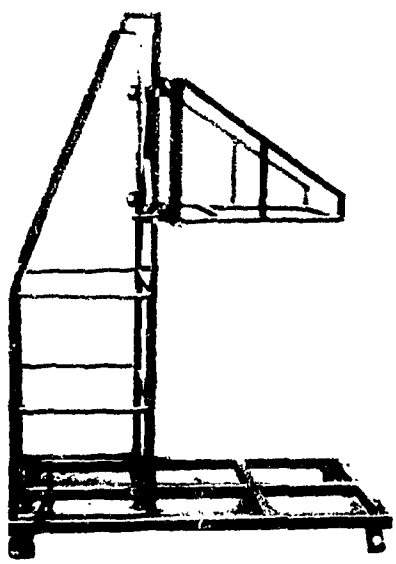

Fig. 8 Photograph of detector mounting system for use with the scanning bed in imaging large animals and patients.

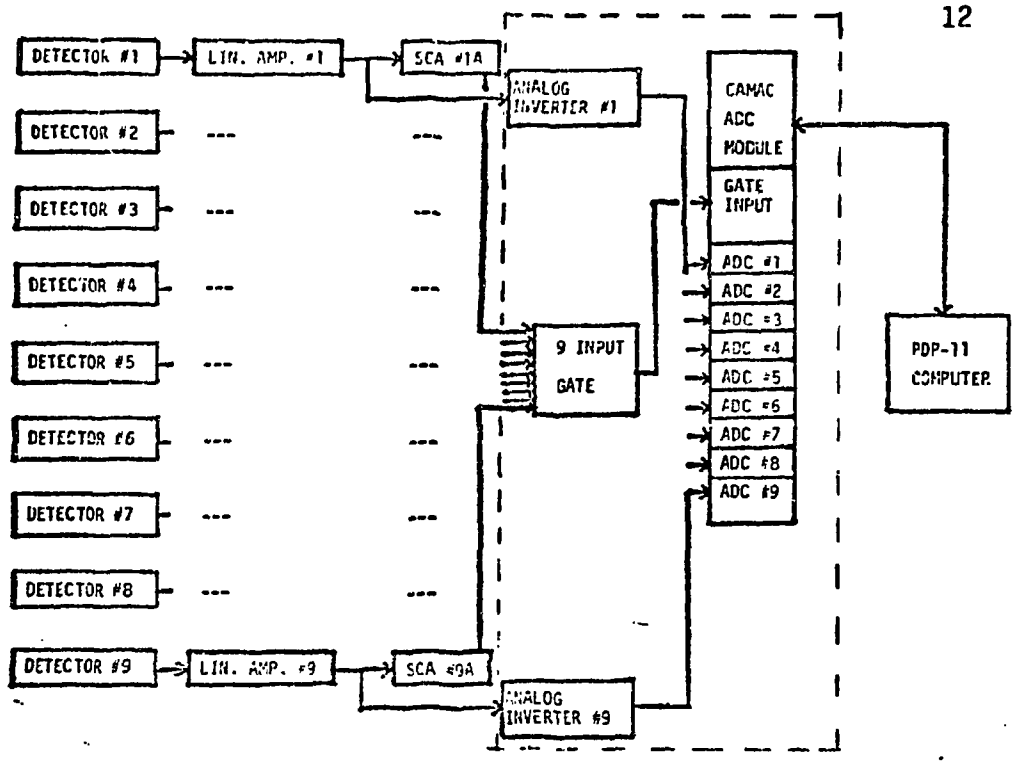

9 A. Block diagram of multiple ADCs in CAMAC for simultaneous collection of multiple energy peaks from multiple detectors.

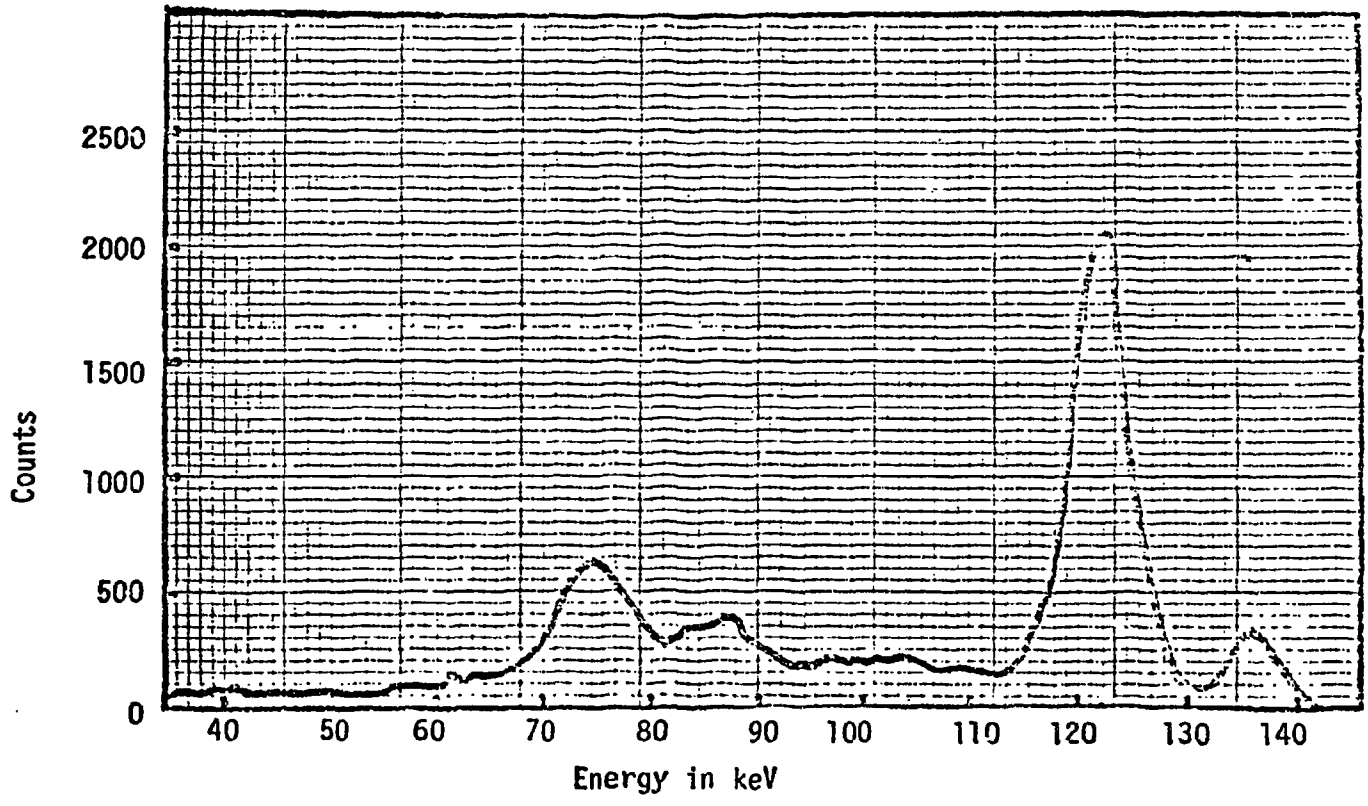

9 B. Energy spectrum collected from a Co-57 source with a single coarse resolution germanium detector to demonstrate capability of system shown at top. SCA window was set to include energy range from 35 to 145 keV.

the computer. A flag is set by the ADC module indicating the particular ADC that has the value to be read. Since the data rates from the individual detectors are not extremely high, the probability of chance coincidences will be small. If this becomes a problem, the SCA pulses can be used to determine the detector from which the event came by means of a CAMAC interrupt register module. An experimental evaluation was performed with a single Ge(Li) detector with relatively poor resolution, not one of the 9 detectors in the intrinsic array, and a LRS 12 input peak-sensing ADC CAMAC module obtained on loan to study the feasibility of this concept. Figure 9 shows an energy spectrum obtained from a Co-57 source and clearly demonstrates the capability of this system. The SCA window was set to include the entire spectrum of energies from 35 to 145 keV.

In Figure 10 are shown images of a thyroid phantom containing Tl-201 that were obtained with the germanium system and with two Anger scintillation cameras utilizing the 70 keV peak of Tl-201 to test the imaging ability of the system at low energies. From the images it is observed that the spatial resolution of the system is comparable to that of our highest resolution scintillation camera, the Ohio-Nuclear mobile camera at this energy.

An experiment was conducted to test the germanium system for the simultaneous imaging of multiple isotope distributions in a situation in which the energy spectra would interfere with each other when measured with NaI(Tl). The isotopes chosen were Tc-99m (140 keV) and Tl-201 (70 keV). In a clinical situation these two isotopes could be used in imaging and diagnosing a patient with myocardial infarcts. A region of infarction would appear as an area of increased uptake on a Tc-99m pyrophosphate image and an area of decreased uptake on a Tl-201 image. The simultaneous imaging of these two isotopes is difficult with currently available NaI (Tl) because scattered photons from Tc-99m may be detected as primary Tl-201 photons. A diagram of the phantom used and the images obtained are shown in Figures 11. The volume was filled with Tl-201, one vial with water, and the other with Tc-99m. The Tc-99m activity was 50% of the Tl-201 activity. Both systems imaged the Tc-99m distribution satisfactorily. The Tl-201 images show that a void can be imaged with the camera only in the absence of Tc-99m in the void whereas the germanium system images both voids quite well. Thus the germanium system should be very useful in the simultaneous mapping of multiple distributions such as used in this study.

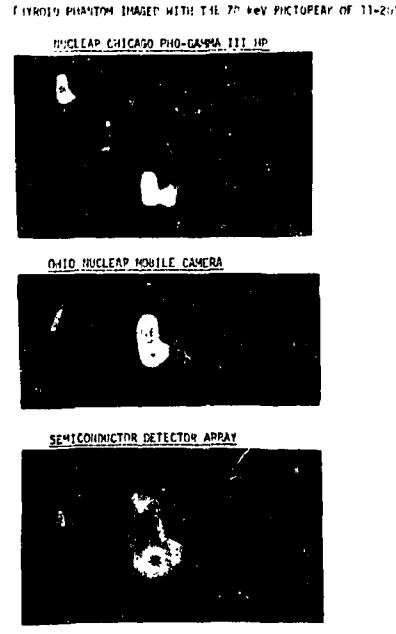

Fig. 10 Photograph of scans of the Picker thyroid phantom imaged with two scintillation cameras and the intrinsic germanium system. The phantom contained Tl-201 and SCA windows were set on the 70 keV peak.

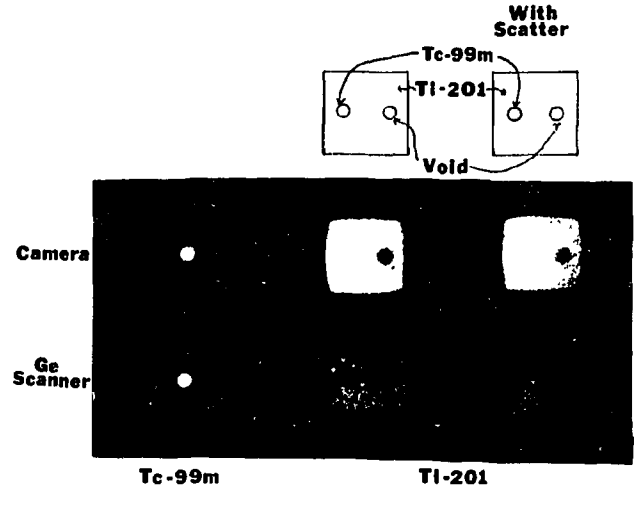

Fig. 11 Photograph of images obtained with the Ohio Nuclear mobile camera and the intrinsic germanium system of a dual isotope distribution of Tc-99m and Tl-201.

4. CAMAC: Design of Autonomous Crate Controller

During the past year we have worked with engineers at Fermi National Accelerator Laboratory (FNAL) who have designed an autonomous CAMAC crate controller.

We have just received on April 22, a prototype version of this controller to evaluate in our environment. The system which we have received is based on the Intel 8080 microprocessor and is diagrammed in Figure 1. The microprocessor controller is programmed to perform the appropriate functions by means of the RS-232 module. This module allows program instructions to be sent to the microprocessor over a standard telephone line from any system capable of driving a computer terminal such as a teletype. This allows us to operate the crate from any of our available computers, i.e., Sigma 7, PDP-9, or PDP-11. Thus, this is the first step in making CAMAC a common data collection means in our laboratory.

At present the RS-232 module is the only means of transferring data as well as programs to and from the microprocessor in the crate controller. At the 1200 bit/second rate which is the frequency used by the majority of our RS-232 ports we will be able to test the utility of the autonomous crate controller with slow data rate procedures such as scintillation probe and rectilinear scanner studies. This will, however, allow us to thoroughly test the concept of distributed data collection systems in a clinical environment and will permit the collection of dosimetry data from our whole body scanning systems.

When used as a data collection system the Intel 8080 microprocessor is programmed just as any other computer with CAMAC would be. It controls the timing of the reading of the scaler modules, and the collection of positional information from rectilnear scanners through encoder follower modules. The data are collected and compressed by the 8080 and sent via the RS-232 module to the master computer to which it is connected.

We are awaiting an updated version of the Intel cross assembler which we will implement on the University's Sigma 7 computer. Once this is accomplished we will begin the actual operation of the autonomous CAMAC crate in our laboratory.

The RS-232 access to the autonomous crate is a restriction that is not realistic for our enviornment for routine use. Thus, we have planned an expansion of the concept which will allow fast transfer of data. This concept is shown in Figure 2. The program or primary control of the Intel 8080 will still be via the RS-232 port but the data collected will be sent back to the control computer (in our case a PDP-9) via a high speed link which will enter the latter through direct memory access port. We are currently designing the detailed specifications of this hardware for the PDP-9. The non-DMA port on the 8080 is in the final stage of implementation at FNAL and will be borrowed to test our PDP-9 DMA port. This module will, however, tie up the CAMAC data way and the Intel 8080 when transmitting data so that we are also planning at the present time the design of a similar module to perform direct memory access of the 8080 and which will not have these disadvantages.

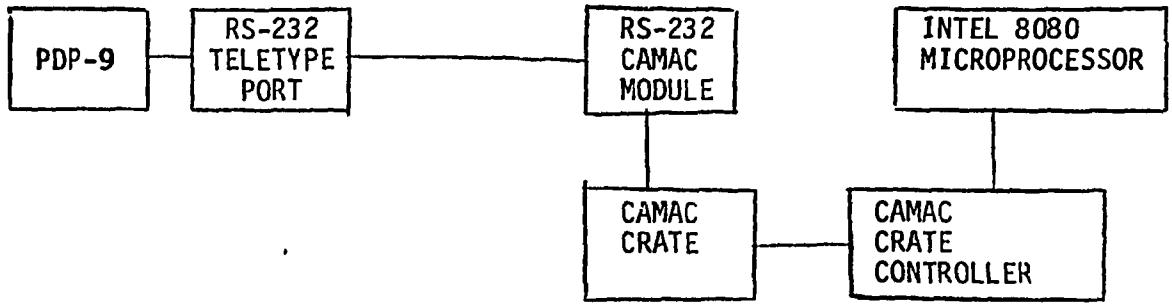

Figure 1. Block diagram of the autonomous CAMAC crate controller system based on the Intel 8080 microprocessor.

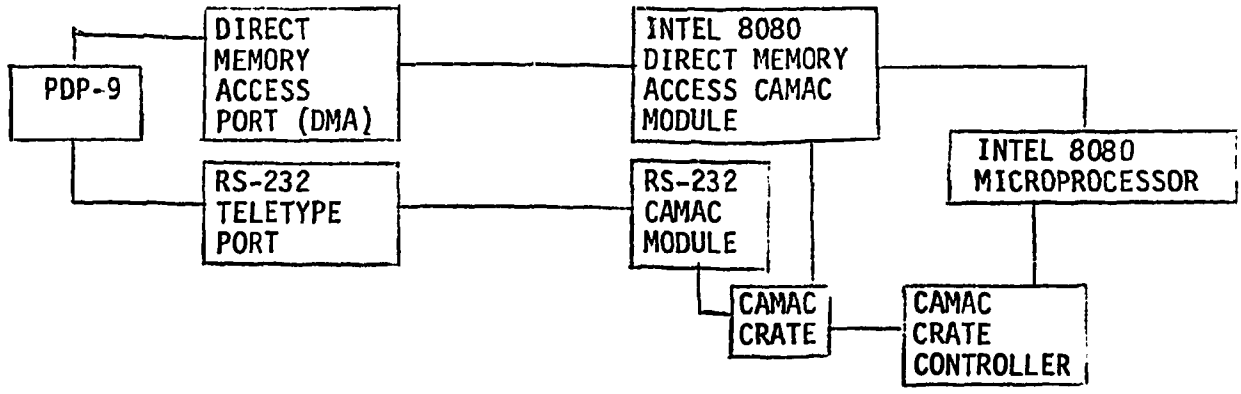

Figure 2. Block diagram of the autonomous CAMAC crate controller showing the high speed, bit serial data link between the DMA of the PDP-9 and the DMA of the Intel 8080 microprocessor.

5. Integrated Anger Camera-Stationary Scintillation Probe

We have developed a system whereby simultaneous data from an Anger Camera and stationary probes are collected from the same patient. Such a system became necessary, since for a number of our studies the camera was inadequate to monitor all of the organs of interest simultaneously. Data presented in section A.2c on I-131 hippuran dosimetry required use of this system. In those studies, the camera was capable of monitoring the kidneys, but the field of view was not able to include the bladder and an adequate blood pool. Thus, probes were directed at the bladder and heart for these measurements.

A block diagram of the integrated camera/probe data acquisition system is shown in Figure 1. An alternate system has also been developed which differs from Figure 1 in that both the camera and probe systems are interfaced via CAMAC. Figure 2 shows an example of the data obtained from the integrated system from a patient receiving an I-131 hippuran renal study at 10 days after renal transplantation.

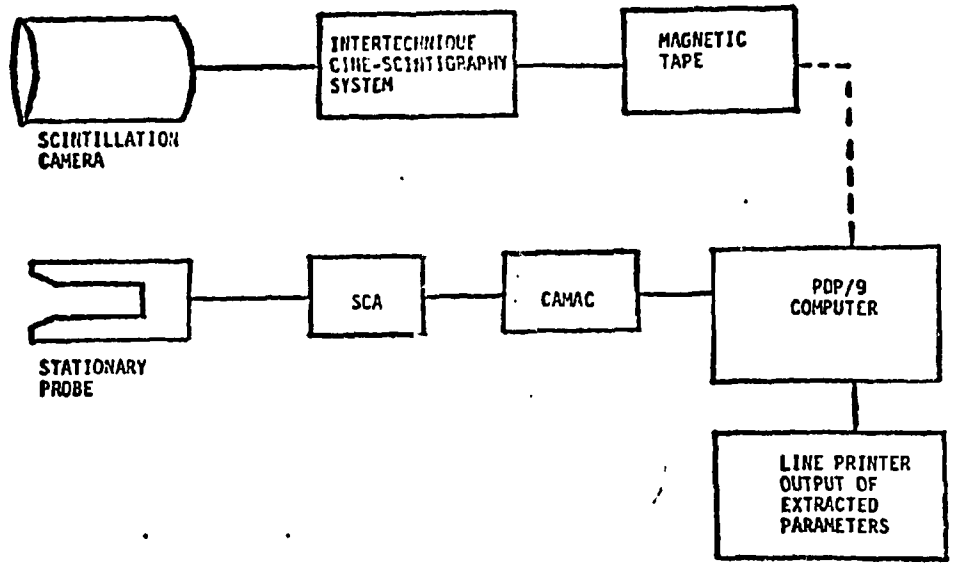

Figure 1. Schematic of Combined Scintillation Camera Stationary Probe Data Collection System

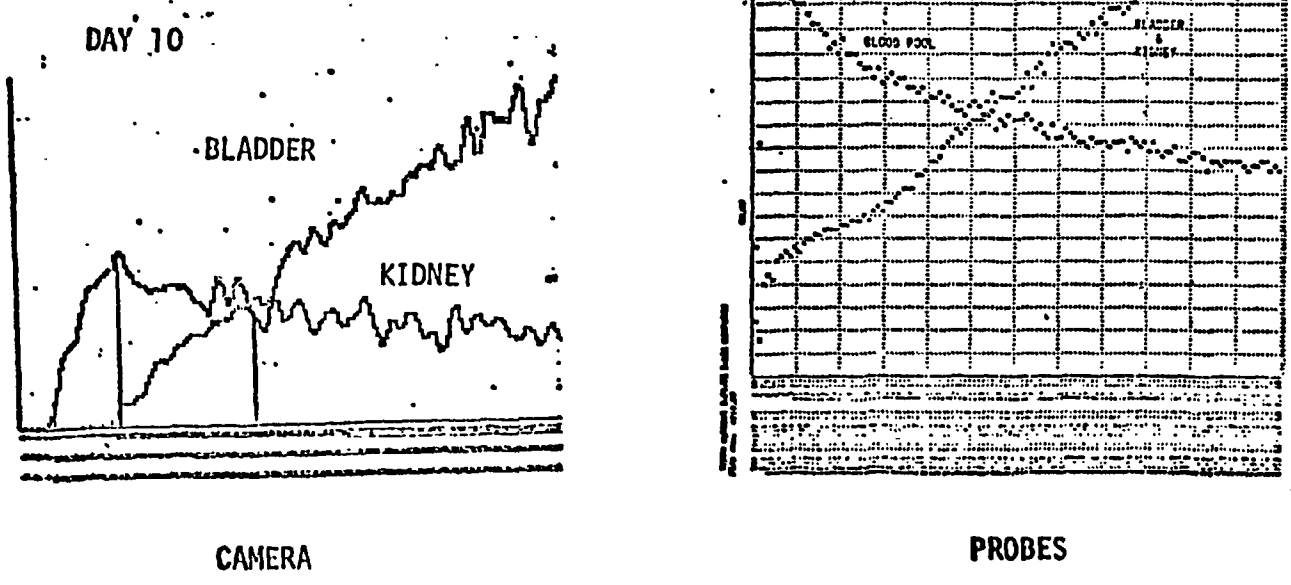

Figure 2. Combined Camera/Probe Renogram Study

6. Video Line Buffer Display System

A new interface for the computer generation of high resolution gray scale images has been designed and built. This interface, called a video line buffer (VLB) links the PDP-9 computer to a multiple track video disc recorder. It contains a high speed bipolar 512 x 10 bit random access memory, a fast 10 bit digital-analog converter, and a logic to synchronize the memory with the video disc.

Data representing a single horizontal video line are loaded into the memory, with up to ten bits of gray scale information at each point and up to 256 points per line. When the memory is filled, the computer loads the interface with a nine-bit number representing the video line at which the data is to be written. When timing signals from the video disc indicate the disc is positioned at the proper line, the memory is dumped onto the video disc at a 5 MHz rate. A complete video picture (525 lines of 256 x 10 bit pixels) can be written in about eight seconds.

This video line buffer is in the final stages of development, and the images presently produced are far superior to those of the scan converter display used previously. As each line of data is acquired, monitor images of anterior and posterior views are displayed on a single video frame. This gives the investigator confidence that the total system is working and data are in accord with expectations. After the study is finished the high quality image permits interaction to identify regions of interest by use of a joy stick, and also is useful for organ volume calculations. The system we have developed for these interactions is indicated in Figure 1. As an example of the quality of this display, images of a liver and spleen obtained from the scintillation camera are shown in Figure 2. This system will also be useful as a monitor for computerized image processing as shown by the example in Figure 3. This is the same scan as shown in Figure 2 after processing using an expanded contours algorithm. Adequate resolution is available for displaying sixteen scintigraphic images on the video frame as shown by the brain bolus images in Figure 4. A video disc remote control located in the scan reading room allows physicians to review computer-processed patient studies. Dynamic studies with multiple images may be played back in forward, reverse, or stop-frame modes to aid in interpretation.

Since data can be written on selected video fields, the VLB has a potential for producing stereoscopic displays. An image to be viewed by the right eye can be written on one field and the left eye image on the alternate field. When viewed through a shutter synchronized with the video frame rate, the image will appear to be stereoscopic. We have on loan from Honeywell a pair of electro-optically switched glasses which we will evaluate in this application for improving 3D visualization of emission distributions viewed from different angles with the Anger camera.

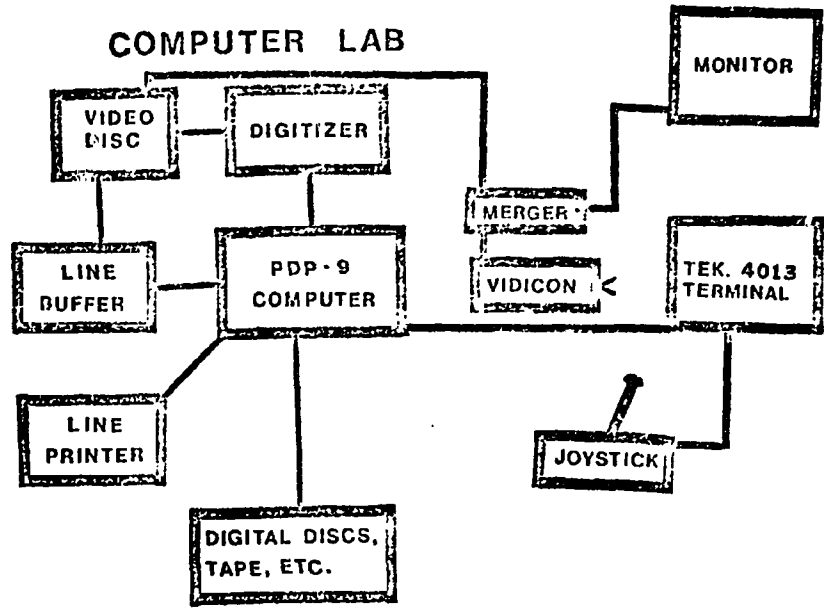

Fig. 1 Block diagram of video electronics configuration.

Fig. 2 Photograph of a liver and spleen scan imaged with the scintillation camera and photographed from a video display produced by the video line buffer.

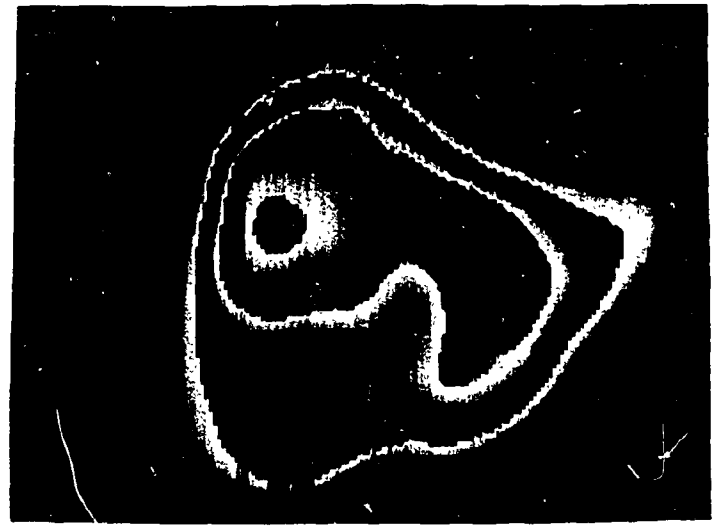

Fig. 3 Photograph of the same scan as shown in Fig. 2 after computer processing with an expanded contours algorithm and displayed with the video line buffer.

Photo not included due to

inadequate photographic reproduction.

Fig. 4 Photograph of 16 frames of a brain bolus displayed with the video line buffer.

b. Software Development
1. Simulation and Modelling

We are continuing to develop and test new kinetic models in an effort to understand better the total body and organ retention of medically administered radioactive materials. Solutions to these models have been sought generally through the use of Berman's SAAM 25 computer program. Our efforts are being directed toward improving model accuracy through the use of external quantitative measurements as supplemental to routine kinetic data. Models are currently being used to analyze data from studies of iron, I-131 hippuran, I-131 Iodocholesterol and iodine kinetics in addition to a number of new radiopharmaceuticals. The details of these models and model calculations will be discussed in the succeeding sections dealing with the specific material.

As a member of the MIRD task group to gather data on Fe-59 dosimetry, we are using the Vanderbilt SAAM-25 iron kinetics model to describe the kinetics of normal and abnormal subjects studied at Vanderbilt and at the University of California. Data from the two laboratories are being merged and the resulting dosimetry information will be published as a MIRD pamphlet.

2. Multi-instrument Executive for Data Collection and Display

We are using the executive program as described in detail in the 1975 proposal for routine data collections. We have not, however, expanded the executive program as proposed there. This is a result of 2 unforeseen occurrances. The first of which was that the hardware system, i.e., the I/O bus structure of the PDP-9 and the multilevel interface to the CAMAC crate, is limited in that it is unable to successfully sustain high data rates without occasional erros due to marginal timing. The second reason for our not expanding the executive was the loss of the programmer who was responsible for this software system. We were unable to dedicate other personnel to the task and have therefore simply maintained and operated the system as configured at the time of the 1975 proposal.

3. Sharing of Computer Programs in Nuclear Medicine

During the past year, we have received and distributed a number of computer programs for the quantitation and analysis of radioisotopic spectral and image data. We have continued to work with Dr. Berman and Mrs. Weiss to help distribute the NIH Simulation and Modelling Program Package (SAAM) to users with 32-bit computers. To date we have supplied copies to four medical centers. We will continue to help introduce new users to the capabilities of the SAAM Programs for the analyses of kinetic data and the calculation of radiation absorbed doses.

During the past year, we have worked with the personnel of the Biomedical Computing Technology Information Center (BCTIC) in Oak Ridge to develop a directory of nuclear medicine computer users. The directory will be published in July 1976. At present, the directory contains descriptions of over 80 U.S. and 20 foreign installations where research is being carried out in the application of computers to nuclear medicine problems. The directory should greatly facilitate the interchange of software packages in the future.

c. Correlation Studies between Calculated and TLD Measurements of Radiation Dose-Applied to Tc-99m Sulfur Colloid Liver Scanning

The purpose of this research is to compare the radiation dose calculated from "standard man" absorbed fractions (MIRD Pamphlets #5 and #11) to actual measured patient dose, in order to evaluate the range of deviations observed in different diseases and to evaluate the validity of the model calculations in idealized circumstances. This project compares the calculated dose to a LiF target on the patient's skin to that measured with LiF TLD's. The source organs are the liver and spleen, each containing Tc-99m sulfur colloid. In order to evaluate the model, both the dose measurements (TLD) and patient activity measurements must be accurately made; otherwise discrepancies due to the model will be obscured by measurement errors.

Careful evaluations of all measurements had been previously made, and a sizable error noted. We proposed several steps to find the cause(s) of error; these steps have been performed, the cause of error discovered, and the large systematic error eliminated. Also, sufficient patient data have been obtained to evaluate the model. As will be seen below, these data showed the discrepancy between measured and calculated dose ranging from slight (<5%) to rather large (factor of two), depending upon the size of the patient relative to the model. A summary of the methods and results will be given here; details can be found in the appendix (J.P. Jones, Ph.D. Thesis, Vanderbilt University).

The cause of the large systematic error was traced to the TLD calibration. This calibration was done by exposing TLD's on a lucite cube containing Tc-99m; the dose was computed from absorbed fractions specially calculated for this geometry by W.S. Snyder and J.W. Poston of ORNL, and the known activity within the cube. It was also found, by making a cross-check between our laboratory and ORNL, that the activity determinations were fairly accurate (to within 8%). Thus, the absorbed fractions used for these studies were incorrect.

We also attempted to determine whether the error in the absorbed fractions was computational or experimental (i.e., non-uniform distribution of activity in cube caused by adsorption of activity on cube walls). Our results indicated the former, but did not prove this, so it was decided to discard the cube and calibrate the TLD's by another method. This method was to expose the TLD's to a radiation source whose output we were very confident of, which was a 100 mCi Cs-137 source. However, Cs-137 gamma rays have a much different energy than those from Tc-99m, so we needed to check for possible energy dependence of the TLD response.

This was done by repeated TLD exposures to the Cs-137 source, as well as repeated exposures to "point" sources of high-activity Tc-99m sources (200 mCi - 700 mCi). The response to each isotope was expressed as counts/mrad to LiF (as opposed to counts/milli-roentgen), and found to be no more than 6% different for the two isotopes. We feel the actual difference to be less than this, but the widely different photon energies emitted by Tc-99m (18.5 keV x-rays and 140 keV gamma rays) precluded more accurate measurements. (The x-rays are intense enough to deliver a dose comparable to the gamma ray dose.) Therefore, the TLD's were calibrated for the patient studies using the Cs-137 source.

The exposures performed on the MR. ADAM phantom at ORNL were reanalyzed using this calibration method, and gave the excellent agreement with the Monte Carlo calculations of Dr. Poston and his co-workers as shown in Table I.

Further patient studies were then performed; the results are shown pictorially in Figure 1, and listed in Table II. In Figure 1, the solid line represents equality between the calculated and measured doses, and the dashed lines represent a 30% discrepancy in either direction. The error bars represent a 5% uncertainty in the measured dose (determined by uncertainties in MR. ADAM experiment and scanning techniques). Thus, discrepancies of 15% or less may well be due to measurement errors, but 30% or more are due, at least in part, to real differences between the model and patients. While it is important to see that the discrepancies are often 30% or less, it is also important that every patient who had a clearly larger calculated dose was either larger than average in size, or had an abnormally small liver due to disease. In addition, every patient who had a clearly smaller calculated dose was of smaller than average size, or had a relatively large liver. This is what one would expect, because the applicability of the model to each patient depends upon the relative amounts of attenuating tissue between the liver and TLD's for the patient and model.

The numerical results are shown in Table II. The column labelled "Extrap" is the total liver and spleen activity extrapolated back to the time of injection (to check the accuracy of the measured activity, and hence, the calculated dose). The "patient's dose" was 3 mCi in each case; the extrapolated values are less than this because about 0.5 mCi remains in the syringe after injection (even after flushing the syringe with the patient's blood, as verified by direct measurement), some of the injected activity is taken up by other organs (e.g., bone marrow), and some free pertechnetate is present in the colloid preparation. Thus, the extrapolated values seem reasonable, except for patients G, J, and L. For patients J and L, the larger values resulted because of technical difficulties with the first injection, so a second injection was given. For patient G, the reason for the low extrapolated value is not known. Perhaps less activity was injected than intended, or perhaps the colloid preparation contained a larger amount of free pertechnetate. In any event, this patient was of average size, had a normal liver scan, and showed good agreement between the measured and calculated doses, so this extrapolated value may be correct.

To summarize, we observed agreement to within 30% in most cases studied, although discrepancies up to a factor of two were noted. Discrepancies tended to be such that measured doses were less than predicted by the model. This may be due to larger livers on the average in abnormals than in normal patients. Patient sizes studied ranged from 5'5", 120 lbs, up to 6'0", 220 lbs, although patient height and weight were not found to be good indicators of the discrepancy, since the size and medical condition of the liver was also a factor. Patient medical conditions included normal, Hodgkin's disease, cirrhosis, and cancer, but these could not be related to the discrepancy, either, since the liver could be normal at certain stages of these diseases. It thus appears that the model is quite accurate in most cases, but one must be aware that appreciable discrepancies can occur. This is very important with smaller patients, because a large underestimate of true dose is a serious dosimetry error.

TABLE I

RECALCULATION OF MR. ADAM EXPERIMENTS

Calibration Exposure to ^{137}Cs				MR. ADAM Exposures			
"Organ"	Dose (mrad)	TLD Reading (counts) (Corrected for different sensitivities)	Dose/count (mrad/count)	Ave.TLD Reading (counts)	C.V. (%)	Ave.Dose (mrad)	R_{exp} ($\times 10^{-14}$ rads/photon)
Liver	284	729	0.389	901	1.48	351	5.30 ± 6.5%
Spleen	284	729	0.389	82	4.40	31.9	0.375 ± 9.4%

Computer Calculated Values of R ($\times 10^{-14}$ rads/photon)	Ratios of R Values
Liver 5.305 ± 12.2%	5.305/5.30 = 1.00
Spleen 0.4033 ± 26.1%	0.4033/0.375 = 1.08

TABLE II

PATIENT RESULTS

Patient ID	Calculated Dose (mrad)	Measured Dose (mrad)	Cal/Meas	Extrap. (mCi)	Top/Bot	d (cm)
A	47.6	41.2	1.15	2.24	0.90	23.1
B	85.7	83.0	1.03	2.29	1.01	25.8
C	50.3	46.5	1.13	2.27	1.48	24.3
D	44.2	42.7	1.03	2.28	3.29	23.8
E	33.5	47.1	0.71	2.30	1.12	22.1
F	43.2	97.2	0.45	2.16	1.47	16.9
G	27.4	29.1	0.94	1.53	1.49	22.4
H	33.7	25.3	1.33	2.27	0.90	25.6
I	60.1	36.0	1.67	2.38	1.20	26.6
J	117.8	95.1	1.24	4.58*	0.85	24.3
K	111.9	118.2	0.95	2.38	1.27	22.3
L	82.6	54.3	1.52	4.42*	1.18	26.2

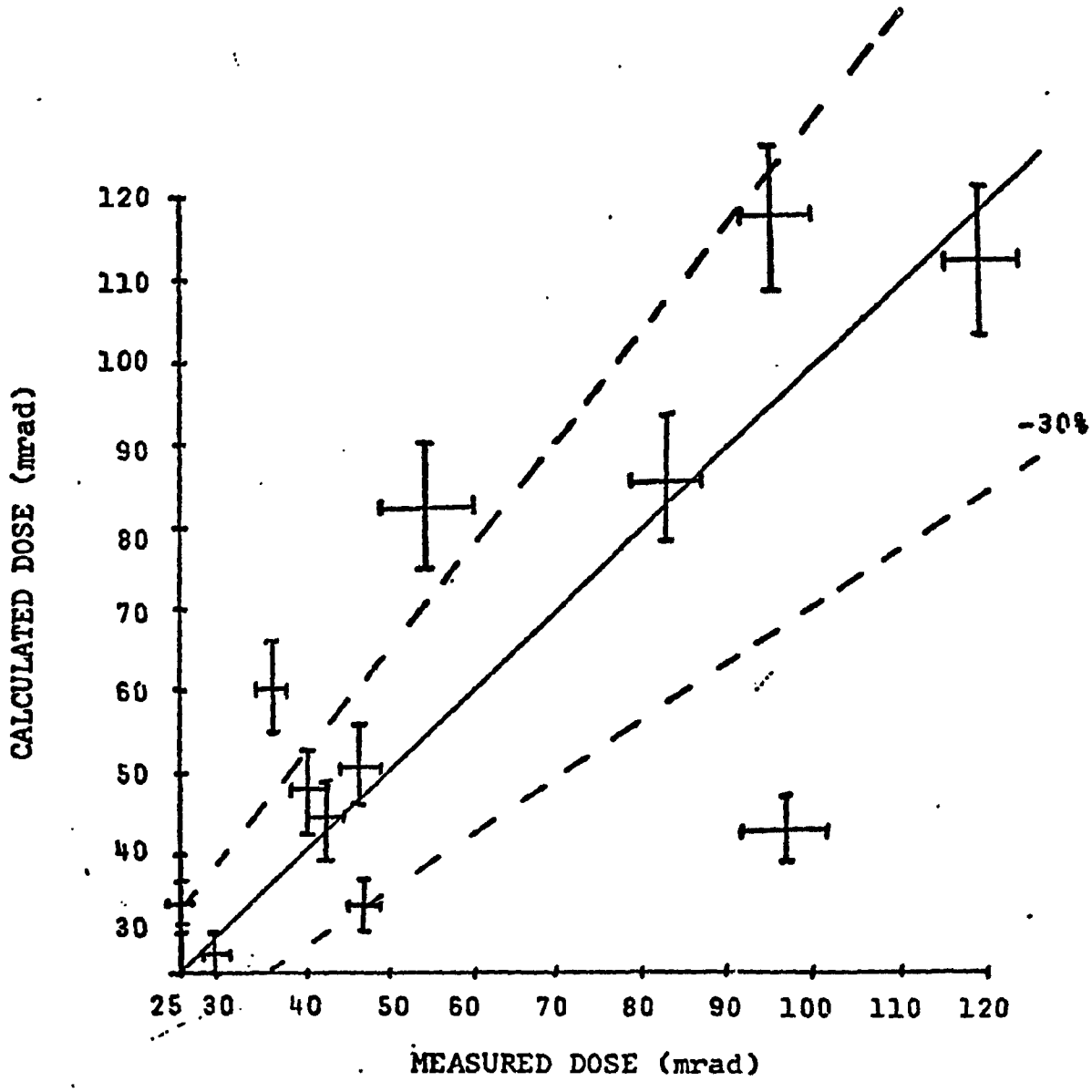
CALCULATED DOSE (mrad)
120
110
100
90
80
70
60
50
40
30
25 30 40 50 60 70 80 90 100 110 120
MEASURED DOSE (mrad)
-30%

FIGURE 1

d. Positron Time-of-Flight System - feasibility study

Experiments have been done investigating the feasibility of time-of-flight positron (TOF) imaging in clinical nuclear medicine. This project was a joint effort between the Division of Nuclear Medicine and the Nuclear Physics Group here at Vanderbilt University. It has resulted in a masters thesis by William Dunn, appended to this progress report.

The use of positron time-of-flight imaging is conceptually attractive though technically difficult. The two annihilation quanta resulting from the annihilation of a positron with an electron are emitted in opposite directions with the speed of light. If one can detect the difference in arrival time of the quanta at two detectors positioned along the axis of the oppositely directed quanta, one determines uniquely the x, y, and z position of the annihilation event. The possibility of tomographic imaging is apparent.

Using state-of-the-art nuclear electronics* and detectors shown in Figure 1 we have obtained spatial resolutions of approximately 2.5 cm with spatial precision of <4 mm. Experiments on a phantom (Figure 2) consisting of bars of activity in a sea of background activity (5:1 concentration) yielded the image shown in Figure 3. The first image is the unprocessed TOF image. The second is with 20% background subtract and the third is a γ-camera image taken from above the phantom. Note that all the bars can be distinguished. We have also analyzed what minimum number of counts are necessary, at our present resolution, to determine that two objects are spatially separated. We have found that <30 counts in the peak channel are necessary. This nubmer will, of course, go down as spatial resolution improves.

Our present sensitivity with Na-22 in water bath with detector separation of 15 cm is 5 cpm/μCi (25% window). Using a multiple detector configuration (such as 2 rows of 4 detectors on either side of the head) a scan of a head could be completed in 25 minutes obtaining ~50 counts in a peak resulting from a 5 μCi/ml hot spot. A 10 mCi administered dose might result in this concentration in a hot region. This is probably not clinically useable at the present time.

We feel, however, that several improvements in TOF imaging are on the horizon which may lead to a more useful device. Significantly faster scintillors are now becoming available. NE 238, a liquid scintillator sold by Nuclear Enterprise, Inc., has recently been developed and appears to have much better time characteristics (factor of 2) than the NE111 which we currently are using. Micro channel-plate phototubes may also become available shortly, with timing characteristics a factor of 3 better than the 5 stage RCA GaP tubes we are now using. Further, some work is being done with fast inorganic scintillators which would have higher densities than plastics leading to better efficiencies.

All of these pending developments lead us to believe that TOF positron imaging having adequate sensitivity and spatial resolution near a centimeter may be possible within the next few years.

---

*The photomultiplier tubes were kindly provided on loan from RCA, the constant fraction discriminators were kindly provided on loan from ORTEC.

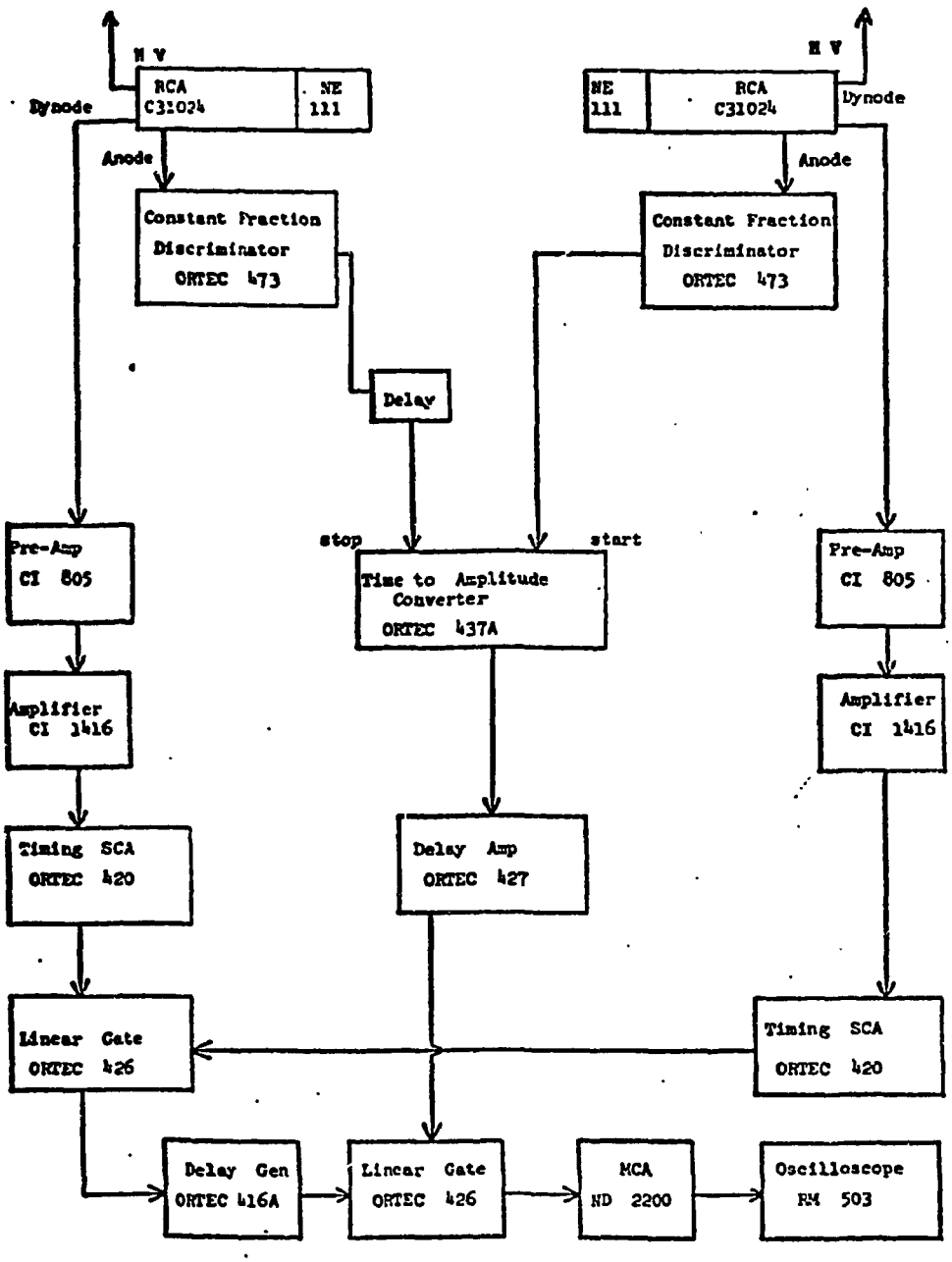

Fig. 1 Block diagram of Positron Time-of-Flight Apparatus

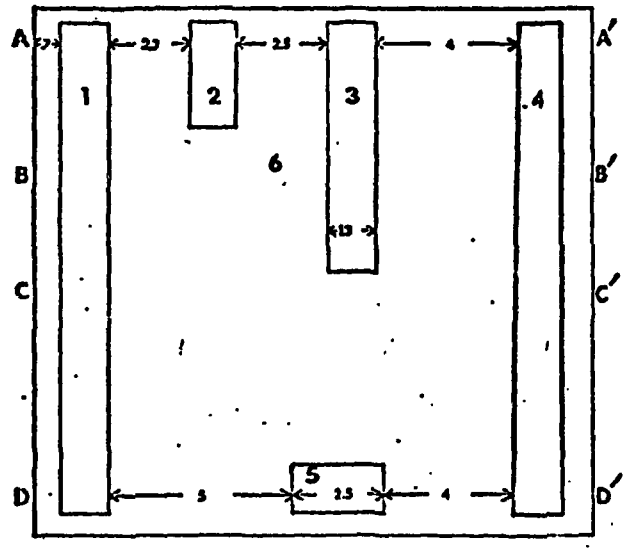

Fig. 2 Schematic of phantom. Regions 1-4 are regions of increased activity. Region 6 has less activity. All dimensions are in centimeters.

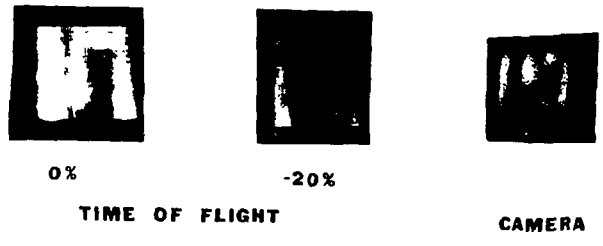

Fig. 3 Time of Flight tomographic image and a comparative scintillation camera image taken from above the phantom.

2. Specific Projects
   a. Dosimetry of New Tc-99m Labelled Lung Scanning Agent in Abnormals

Early studies suggested that the retention of labelled human serum albumin microspheres in the lungs might be longer than with previously used labelled macroaggregates. If so, they would deliver an increased radiation dose to the patient as well as occlude vascular channels to a greater extent. With the aid of the quantitative whole body scanner we have measured the total body content as well as the content of the lungs, liver and spleen as a function of time. Several commercial kits for making Tc-99m macroaggregated albumin and albumin microspheres administered for routine diagnostic lung scans were studied.

During the past two years we have carried out studies on 12 normal volunteers. Each volunteer was administered 500 uCi (one-quarter of the clinical scan dose) of the Tc-99m labelled compounds. Whole body scans and blood samples were taken at 1, 3, 6, and 24 hours after injection. From these data the biological retention and cumulative activity curves $\left(\tilde{A}\ \frac{\text{uCi hour}}{\text{uCi}}\right)$ for the total body, lungs, liver, spleen and blood have been determined. Tables I and II summarize the results of the quantitative whole-body scans showing the group mean values of the total-body distributions of the materials as a function of time.

Dose estimations assuming uniform distributions of the materials in the lungs and total body had been determined earlier and are summarized in Table 3 and 4. To our surprise, the dose to the lungs and the effective T-1/2 is greater for Tc-MAA than for microspheres. Further analysis of the data has allowed us to determine the biological retention functions of the liver and spleen for each of these materials. They were found to be as follows:

Tc-99m Albumin Microspheres

$$\text{Liver} = 0.07\ (1 - e^{\frac{-0.693}{12.5}\ t})$$

$$\text{Spleen} = 0.04\ (1 - 3^{\frac{-0.673}{5.0}\ t})$$

Tc-99m Albumin Macroaggregates

$$\text{Liver} = 0.05\ (1 - e^{\frac{-.693}{10.5}\ t})$$

$$\text{Spleen} = 0.05\ (1 - e^{\frac{-.693}{7.5}\ t})$$

The cumulative activity $\tilde{A}$ was determined in each case using the above equations. From the cumulative $\tilde{A}$'s the average dose to the liver, spleen and testes or ovaries was calculated assuming uniform source distributions in the liver and spleen. The results of these calculations are shown in Tables 5, 6, and 7.

TABLE I

Macroaggregated Albumin (Group Mean)

Time (hours)	Total Body	Lungs	Liver	Spleen	Blood
.25					2.3 ± 0.6
1	100	86.5 ± 1.8	1.1 ± 0.2	1.6 ± 0.7	5.5 ± 2.6
3	98.1 ± .9	79.6 ± 1.8	1.5 ± 0.2	2.2 ± 0.7	5.2 ± 0.9
6	87.1 ± 2.4	67.5 ± 1.4	2.2 ± 0.3	2.8 ± 0.8	6.5 ± 1.6
24	73.0 ± 14.8	52.3 ± 12.2	4.5 ± 1.2	4.8 ± 1.0	3.2 ± 1.7

TABLE II

Albumin Microspheres (Group Mean)

Time (hours)	Total Body	Lungs	Liver	Spleen	Blood
.25					10.6 ± 2.3
1	100	82.3 ± 4.6	1.9 ± 0.4	1.4 ± 0.5	14.7 ± 2.6
3	98.1 ± 0.9	68.5 ± 4.5	2.8 ± 1.0	2.1 ± 0.6	17.0 ± 3.0
6	81.4 ± 6.0	54.7 ± 3.7	3.0 ± 1.0	3.0 ± 1.0	15.5 ± 2.4
24	70.4 ± 12.0	45.1 ± 6.5	6.8 ± 2.9	3.6 ± 1.1	8.4 ± 1.5

Table III

$\frac{\text{rem}}{\mu\text{Ci Administered}}$

Tc-99m Albumin Macroaggregate

Source / Target	Total Body	Lungs
Total Body	3.47	12.03
Lungs	3.48	312.48
Ovaries	4.23	5.63
Testes	2.95	.0047

Table IV

$\frac{\text{rem}}{\mu\text{Ci Administered}}$

Tc-99m Albumin Microspheres

Source / Target	Total Body	Lungs
Total Body	8.30	8.20
Lungs	8.32	212.94
Ovaries	10.12	3.84
Testes	7.04	.0032

TABLE V

Cumulative Activity

$\frac{\text{mCi} \cdot \text{days}}{\text{administered dose in mCi}}$

	Liver	Spleen
Tc-99m microspheres	0.042	0.020
Tc-99m macroaggregates	0.029	0.028

TABLE VI

Tc-99m Microspheres

$\frac{\text{m rem}}{\text{mCi administered}}$

Target \ Source	Liver	Spleen
Liver	4.62	0.47
Spleen	0.92	16.0
Testes	0.06	0.02
Ovaries	0.45	0.19

TABLE VII

Tc-99m Macroaggregates

$\frac{\text{m rem}}{\text{mCi administered}}$

Target \ Source	Liver	Spleen
Liver	3.19	0.66
Spleen	0.64	21.8
Testes	0.04	0.03
Ovaries	0.31	0.27

Below we have compared the results of our measurements with those published in the most recent NCRP publication.

Tc-99m Albumin Macroaggregates

Organ	Vanderbilt	NCRP*
Total Body	12.0	--
Lungs	312.5	207
Liver	-	29.6
Ovaries	5.6	8.5
Testes	3.0	5.2
Red Marrow	---	11.4

Tc-99m Microspheres

Organ	Vanderbilt	NCRP*
Total Body	8.3	--
Lungs	213.0	--
Liver	-	--
Ovaries	10.1	6
Testes	7.0	3.6
Red Marrow	---	13.4

*Draft Report, Committee 32.

To date it has been impossible to obtain a complete set of data from an abnormal subject with pulmonary disease. Abnormal subjects are in general, critically ill and cannot tolerate repeated measurements required for dosimetric investigations. Data taken from routine clinical procedures have been found to be inappropriate for our needs. The only source of abnormal data available to us is from patients having repeated xenon-ventilation studies who have had a single perfusion study. Patients conforming to these restrictions are rare; however, we will continue to look for these studies and will use these data not only for Tc-99m dosimetry but also for xenon dosimetry.

b. Fe-59 Dosimetry - abnormals

In recognition of the need for dosimetry data for abnormal subjects, we have been using our fund of abnormal patients combined with clinical and research instrumentation to collect quantitative information on the metabolic fate of Fe-59 administered intraveneously. During the past year we have carried out detailed kinetic studies on an additional 10 patients. These studies have been in cooperation with Dr. Sandford Krantz of the Department of Hematology and have been an average of 12 - 14 days in duration. Measurements have consisted of daily quantitative whole-body scans, plasma disappearance measurements and daily red blood cell incorporation measurements.

The problems associated with the measurements of the parameters of iron metabolism have been recognized for many years. The sizes of the iron storage pools have been particularly difficult to determine by tracer techniques because of the long time required for the equilibration of these pools with the circulating iron pools. In order to adequately characterize the storage pools of the liver and spleen by means of plasma levels of the radioiron (the most commonly used technique), measurements over extended time intervals would be required. The extended time periods present two major problems: 1) plasma levels or radioiron are extremely low making the statistical errors associated with the measurements large and, 2) measurements over extended periods are not practical for critically ill patients. Critically ill patients receive numerous transfusions of whole blood and packed red cells which tends to alter blood volumes and consequently the estimate of absolute circulating iron levels. Our approach, as described in previous reports, has been to develop techniques for making quantitative external measurement of the peripheral iron storage pools and to combine these data with the measurements of the circulating iron pools in a normalized self consistent manner using compartmental modelling techniques. The ability to measure the turnover of these slowly exchanging compartments directly, rather than inferring their kinetics from plasma clearance and red blood cell incorporation of radioiron, provides additional information on the anatomical distribution of these pools within the body and makes possible more reasonable dosimetric calculations.

The MIRD Committee in the United States has created a task group to gather dosimetric information on the medical uses of Fe-59 citrate. Dr. Price is a member of this task group and we are working in cooperation with the Donner Laboratory of the University of California* to create a single data base. Vanderbilt's SAAM-25 iron kinetics model has been chosen to be used for the calculation of the cumulative organ activity (Ã) for the compiled normal and abnormal studies.

In order to conform to earlier MIRD publications, we have sought to derive analytical expressions for the time activity curves of the various organs and model compartments utilizing the models iteratively derived least square "best" fit values for the intercompartmental flow rates. TABLE I shows the results of these model calculations for a group of abnormal subjects. The model used for these calculations is shown in more detail in Appendix I. By relating the time activity curves of each organ to the model parameters one can easily carry out an integration over time to obtain the cumulative activity (Ã).

*Myron Pollycove (also at San Francisco General Hospital)

Appendix I presents in detail the derivation of the time activity functions for the red marrow and circulating red blood cell compartments as well as the cumulative activity $\tilde{A}$ for each compartment. For the storage compartments each individual patient study was integrated numerically or fit to a sum of exponentail functions and then integrated analytically.

Figure 1 is a plot of the activity curves for a normal subject for the liver, spleen, RBC and red marrow. The parameters used for these calculations are those found for subject Q in Table I. The liver and spleen curves were derived by determining the fractions of the slowly equilibrating stores and the circulating blood pools necessary to reproduce the external measurements. Those fractions were found to be:

$$\text{Liver} = 0.67\ (\text{fast stroes}) + 0.15\ (\text{slow stores}) + 0.26\ (\text{RBC})$$

$$\text{Spleen} = 0.15\ (\text{fast stores}) + 0.15\ (\text{slow stores}) + 0.10\ (\text{RBC})$$

Figure 2 shows the resulting cumulative activity curves $\tilde{A}$ as derived from the time integration of the net activity curves as described in Appendix I. (The $\tilde{A}$ for the liver and spleen are obtained from the $\tilde{A}$'s for the slow and fast storage compartments weighted according to the above equations.) As one might expect, essentially all of the dose to the red marrow is delivered during the first few days in contrast to the RBC compartment which continues to increase.

The radiation dose to the red marrow is of prime importance. We have carried out the calculations of $\tilde{A}$ for the marrow, RBC, liver and spleen for each of the abnormal studies in the manner described in Appendix I. The resulting $\tilde{A}$'s are shown in Table II. Using these values we have estimated the average radiation doses to the red marrow, RBC, liver, spleen, gonads and total body. The results of these calculations are found detailed in Appendix II. The ranges associated with these measurements are shown in Table III compared with available literature estimates.

Table IV summarizes the results of our dosimetric studies on 16 abnormal subjects. We have catagorized the results of the radiation dose estimates with respect to disease state. More complete tables such as this can be used by physicians to estimate what radiation doses might be expected as the result of a diagnostic procedure. Even from this rather small sampling of disease states, strong disease dependence has become obvious.

TABLE I

Fe-59 Dosimetry

Intercompartmental Rate Constants (fraction/day)

	Disease	Plasma to Marrow λ_1	Marrow to RBC λ_2	Plasma to Radid stores	Rapid stores to Slow Stores	Slow Stores to Rapid stores	Rapid Stores to Plasma
A	Hemachromatosis	30.0	0.30	12.0	0.10	0.12	0.82
B	Leukemia	9.6	0.17	6.2	3.0	0.005	0.10
C	Refractory Anemia	29.0	0.15	4.0	0.02	0.001	0.29
D	Follicular lymphoma	8.0	0.30	6.9	3.0	0.005	1.46
E	Intestinal bleeding	15.6	0.10	0.27	0.13	0.27	0.29
F	Refractory anemia (marrow storage)	28.7	0.01	6.16	1.55	0.56	0.74
G	Refractory anemia (liver storage)	4.2	0.07	10.5	0.74	0.01	0.44
H	Refractory anemia	2.7	0.20	6.8	0.45	0.03	0.001
I	RCA(suspected)	6.2	0.13	3.2	0.53	0.04	0.29
J	RCA(remission)	3.8	0.35	3.9	0.37	0.001	0.31
K	Pure RCA	0.65	0.004	4.0	0.73	0.08	0.12
L	Refractory anemia	5.3	0.19	2.7	0.11	0.19	0.18
M	RCA(remission)	24.8	0.14	1.8	13.7	0.66	0.001
N	RCA(suspected)	5.0	0.18	5.0	0.61	0.09	0.001
O	Pure RCA	0.24	0.04	2.3	0.65	0.11	0.001
P	RCA(suspected)	3.78	0.03	4.3	13.7	0.001	12.4
Q	Normal	8.00	0.23	2.3	0.53	0.05	0.20

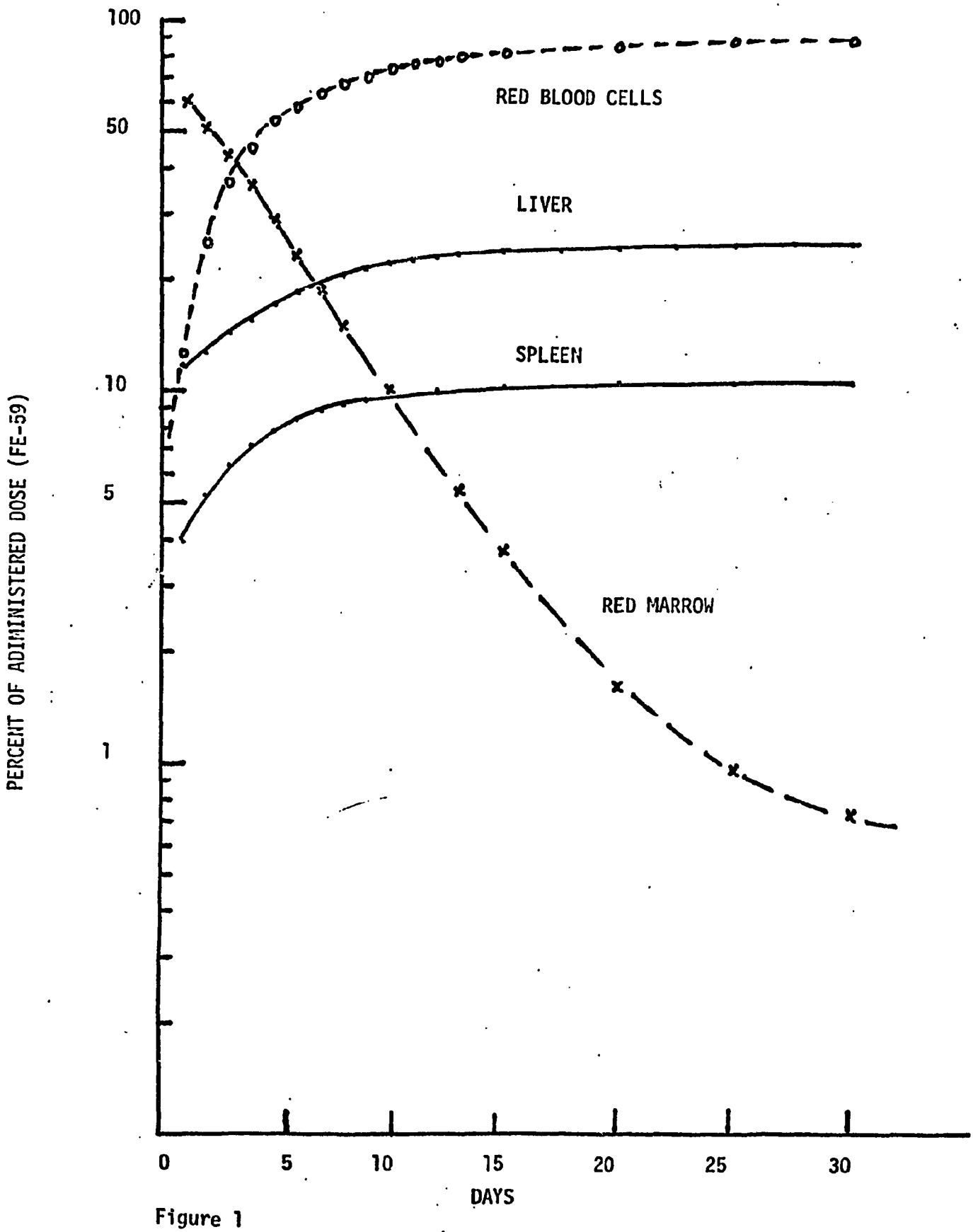
100
50
10
5
1
PERCENT OF ADIMINISTERED DOSE (FE-59)
RED BLOOD CELLS
LIVER
SPLEEN
RED MARROW
0
5
10
15
20
25
30
DAYS

Figure 1

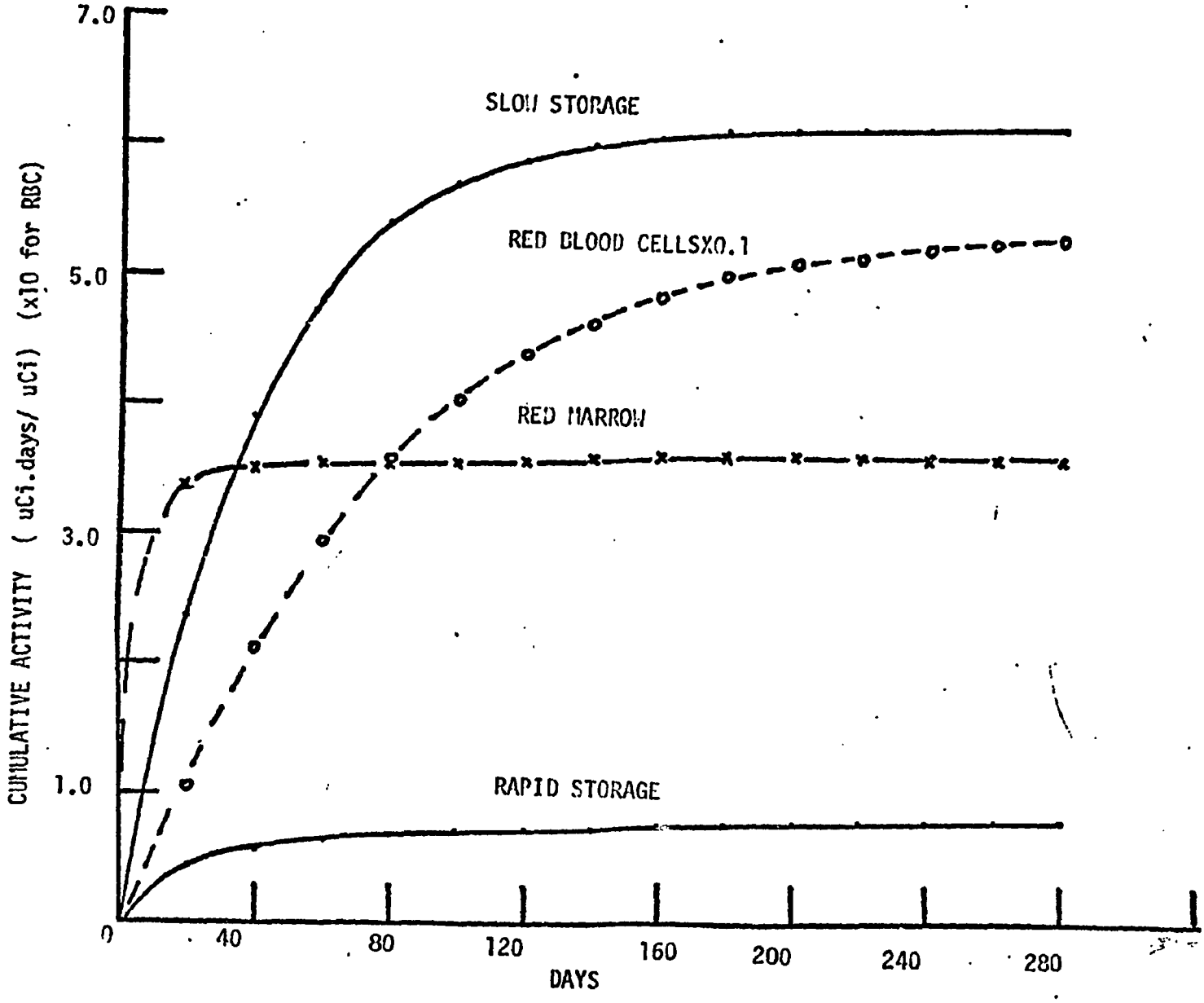
7.0
5.0
3.0
1.0
0
CUMULATIVE ACTIVITY (uCi.days/ uCi) (x10 for RBC)
SLOW STORAGE
RED BLOOD CELLSX0.1
RED MARROW
RAPID STORAGE
40
80
120
160
200
240
280
DAYS

Figure 2

TABLE II

Cumulative Activites Fe-59 Citrate

μCi · day/μCi administered

	A	B	C	D	E	F	G	H	I	J	K	L	M	N	O	P	Q
Red Marrow	2.85	1.73	0.91	2.85	6.67	38.9	1.17	0.37	4.12	1.63	2.57	2.92	1.93	2.04	0.90	5.50	3.66
Blood	55.5	19.0	8.83	55.5	43.3	5.1	5.32	4.82	34.8	37.2	0.67	36.0	17.5	23.9	2.34	10.7	54.7
Liver	8.1	26.0	31.0	13.0	13.0	13.0	52.0	19.5	19.0	19.2	41.0	19.5	13.0	16.2	41.0	26.0	6.5
Spleen	2.6	13.0	13.0	22.0	2.6	13.0	5.2	4.6	2.8	2.6	3.9	2.6	5.2	3.9	5.2	3.9	2.6

TABLE III

Summary of Fe-59 Citrate Dosimetry
in Abnormals
(mrem/μCi)

	Liver	Spleen	Red Marrow	Gonads	Blood*	Total Body
Vanderbilt	77-426	169-1296	8-191	2-28	1-53	11- 35
Berlin (1973)	100	130	-	27	22	22

* non-penetrating dose only

Table IV

Fe-59 Citrate Dose Estimates

for

Various Erythropoietic Diseases

(mrem/μCi)

DISEASE	LIVER	SPLEEN	RED MARROW	GONADS	BLOOD	TOTAL BODY
Refractory Anemia	118 - 258	169 - 762	8 - 191	3 - 20	5 - 36	11 - 28
Hemachromotosis	91 - 426	175 - 313	19 - 37	5 - 23	5 - 53	25 - 36
Leukemia	223	763	24	9	10	24
Folicular Lymphoma	135	1296	43	28	53	35
Red Cell Plasia	114 - 335	169 - 310	14 - 32	2 - 25	1 - 37	15 - 25
Intestinal Bleeding	126	172	52	24	50	25
Normal	77	175	41	23	53	25

c. Dosimetry of I-131 Hippuran in Bi-lateral and Transplant Renograms

In the dosimetry of transplant kidney patients undergoing renal evaluation using I-131 hippuran, four basic categories of function are observed. Patients in the first category show no function, and the hippuran simply distributes itself throughout the body. The second category includes patients with slow renal uptake and excretion, in whom the hippuran resides in the kidney for a relatively long period of time. The third category is those with more rapid uptake and excretion, and the fourth is those with normal function (rapid uptake and excretion). The major dosimetry problem in each category of patients is the determination of absolute renal activity as a function of time.

In our clinic, transplant renograms are performed by injecting 45 μCi of hippuran as a bolus, and collecting gamma camera images at the rate of 6 per minute for thirty minutes. From these, curves of relative renal and bladder activity can be found for the thirty minute period, but more information is needed to find absolute activity. An external probe is also placed over the heart to monitor changes in blood activity, but because of bolus effects, interpretation of the probe curve is not straight forward. The proper interpretation of the early part of the probe curve is important, since this is the only time interval during which the blood activity is known (equals the injected activity).

Of the four categories mentioned above, the second receives largest kidney doses. Unfortunately, it is also the one presenting the most difficult measurement problem. This is because at thirty minutes, the renogram curve over the kidney is still increasing, or at best, it levels off at the end of thirty minutes. Thus, extrapolation of the kidney curve to later times is done with unknown accuracy.

Immediately following surgery, transplant renograms are performed in our clinic routinely three time a week, 48 hours apart and with patients in this category, it is always observed that no appreciable hippuran remains in the kidney after 48 hours. Thus, if one assumes an exponential elimination from thirty minutes post-injection to 48 hours, an approximate upper limit to the kidney dose can be computed. This essentially was the method used; from a knowledge of the injected activity and the probe curve, the blood activity was computed as a function of time. Then, during portions of the kidney curve where bladder activity had not yet appeared, the kidney activity was computed as the difference between injected activity and blood activity. This gave the kidney activity as a function of time up to thirty minutes, and if elimination was observed (third and fourth categories), the curve was extrapolated exponentially from the peak. If elimination is not observed, (category two), the curve was extrapolated exponentailly so that at 48 hours, it had dropped to 0.01 of its maximum value (30 min value).

To illustrate the problems of interpreting the probe curves, a typical one is shown in Figure 1. Each plotted point represent ten seconds of elapsed time, so the initial sharp peak is due to the bolus circulating through the heart and lungs before leaving the chest area. Thus, the drop of the peak is due to activity leaving the heart, but not yet removed by the kidney, and further, the bolus is being spread out,

although it retains a leading edge. In contrast, at later times along the curve, there is no bolus. The drop in counts is due entirely to kidney uptake of hippuran (if no uptake, the curve is flat). In order to relate the probe counts to blood activity, we extrapolate the curve from longer times back to the injection time, using a linear combination of two exponentials, and this extrapolated value is assumed to correspond to the injected activity (see Figure 1). The accuracy of this procedure is not yet clear (we intend to study this point in the coming year), but the technique is expected to give reasonable dose estimates.

To first check that the method of interpreting the probe curves would give reasonable results, it was first applied to several patients with normal renal function, for whom the dose is expected to be small. Then it was applied to various patients in other categories, giving the results shown in Table I. As can be seen, patients with good function accumulated most of their dose within the thirty minute renogram, whereas the situation changes dramatically for those with worse function. Also, patients with poor function tended to have somewhat larger doses during the 30 minute renogram as well, although this tendency was not as clear-cut as with the 30 minute to infinity doses. It should be noted that all the patients with poor function had appreciable (~35μCi of the injected 45 μCi) activity in the kidney at 30 minutes, but the kidney curve was no longer rising, and some excretion had occured. Depending upon the degrees of uptake and excretion, the renal dose to patients with poor function will vary from approximately the1000 mrad calculated here, down to approximately 300 mrad (total body to kidney S-factor from MIRD Pamphlet No. 11) if there is no uptake or elimination . One should also note that these doses are much smaller than the case where all 45 μCi is rapidly taken up but not excreted (≈36 rad), indicating the importance of slow uptake in keeping the dose relatively small.

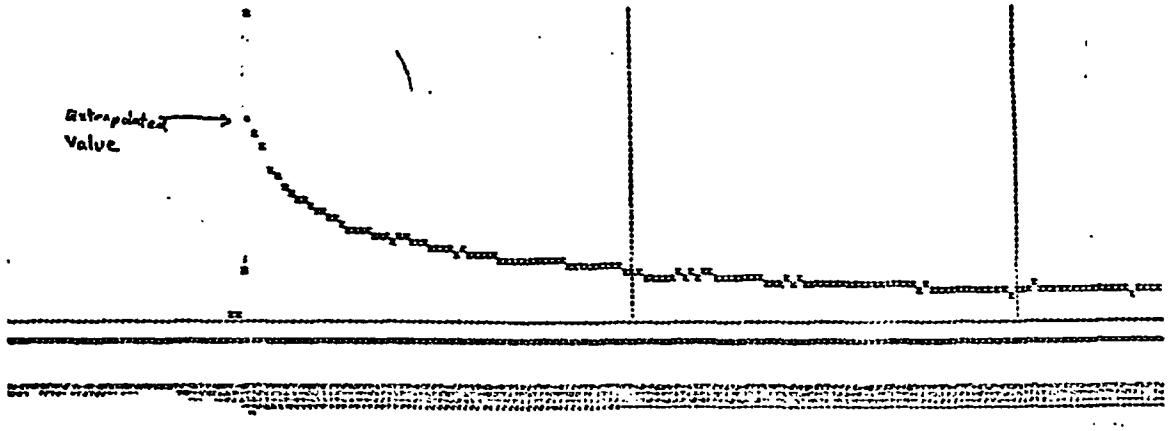

Fig. 1 Typical probe curve.

Table I. Compute Renal Doses for a Representative Set of Patients. (The dose was computed using kidney to kidney S-factor from MIRD Pamphlet No. 11)

Patient	Renal Function	Cumulated Activity (μCi -hr)			Dose	
		0 → 30 min	30 min → ∞	Total	mrad	mrad/μCi
A	Good	6.94	3.60	10.54	32	0.701
B	Good	7.40	4.24	11.64	36	0.798
C	Good	8.57	5.12	13.69	42	0.912
D	Good	12.85	3.24	16.09	48	1.07
E	Fair	8.94	29.74	38.68	116	2.58
F	Fair	9.04	38.18	47.22	142	3.14
G	Fair	9.64	37.07	46.71	140	3.12
G	Improved	7.38	10.35	17,73	55	1.08
H	Poor	10.44	305.66	316.10	951	25.0
I	Poor	9.37	270.63	280.00	840	18.7
J	Poor	12.39	328.87	341.26	1024	22.8
K	Poor	11.33	286.56	297.89	894	19.9

d. Dosimetry of Tc-99m Labelled Pyrophosphates

Much interest has been shown recently inTc-99m Pyrophosphate as both a bone scanning agent and as an agent for assessing myocardial infarctions. Available data indicate that the bone to blood ratio may be improved for Tc-pyrophosphate. To evaluate dosimetry correlates, studied 3 volunteers during the last year according to the protocol shown below. These volunteers were selected from patients referred to the Division of Nuclear Medicine for routine bone scans. After informed consent had been obtained the patients were studied for 48 hours post injection using the whole body counter, whole body scanner, blood samples, and scintillation camera images. These data reveal a multi-component blood disappearance curve and a total body curve consisting of at least two components.

PYROPHOSPHATE PROTOCOL

Step 1. Determine plasma volume with I-125.

Step 2. Inject ^{99m}Tc-pyrophosphate (15 mCi) and collect data as per protocol below.

TIME	BLOOD SAMPLE	W.B. SCAN	W.B. COUNT	PIN-HOLE CAMERA THYROID & ANKLE
15-20 minutes			X	X
2 hours	X	X		
6-8 hours	X		X	X
24 hours	X		X	X
48 hours	X		X	X

The results of the total body and blood measurements are shown in Table I. These data were used to define a two component disappearance curve for the blood and total body content of the Tc-99m labelled pyrophosphate. The parameters (intercept and decay constants) describing the biological retention of this material for three patients are shown in Table II. Patient A was diagnosed as having multiple metastatic lesions from a primary carcinoma of the breast with the bone scan demonstrating multiple areas of increased uptake. Patient B had an increased alkaline phosphatase and evidence of metastatic melanoma. The bone scan was negative. Patient C was diagnosed as having a benign hypertrophied prostate with a negative bone scan.

The first (fastest) components shown in Table II was identified as the portion of the pyrophosphate and unbound Tc that was not taken up by the bone.

The second (slower) component is identified as the bone compartment. With these assumptions the integrated cumulative activity $\tilde{A}$(mCi hours/mCi) for the total body and bone components and shown in Table III for each of the three patients.

The dose equivalents for Tc-99m (rem/μCi day) to the total body, skeleton, testes or ovaries and red marrow from sources uniformly distributed in the total body, cortical bone and cancellous bone have been abstracted from ORNL report 5000 by Snyder, et al and is listed in Table IV. We have identified the slowest component of the total body disappearance curve as the bone compartment, however, we have no way of knowing whether the pyrophosphate is located entirely in the cortical bone or entirely in the cancellous or a linear combination of both. For dosimetric purposes, we have calculated the radiation doses to the various target regions defined, assuming the total amount of radioactive material to be completely in both types of bone thus defining maximum limits of absorbed doses.

Doses estimated in this manner are shown in Table V. Total body estimates ranged from 3.4 to 11.2 mrad/mCi administered. Organs receiving the largest dose were the skeleton and red marrow. The dose estimates to the blood producing marrow ranged from 7.0 to 47.4 mRem/mCi with the maximum dose estimate corresponding to the assumed radioactive distribution being entirely within the cancellous bone. The radiation dose to the skeleton ranged from 10.0 to 62.4 mRem/mCi with the maximum dose resulting from an assumed source distribution in the cortical bone.

Below we have compared the results of our measurements with those published in the most recent NCRP report on Tc-99m polyphosphate.*

ORGAN	mrad/mCi (Vanderbilt)	mrad/mCi (NCRP)
Total Body	3.4 - 11.2	----
Total Bone	10.0 - 62.4	50
Red Marrow	7.0 - 47.4	30
Ovaries	1.0 - 13.8	8
Testes	1.1 - 9.7	6

*Draft of NCRP-32

TABLE I

Abbott Tc-99m Pyrophosphate

Pt #C

Time (hours)	Blood Plasma (% of adm.)	Total Body (% of adm.)
3.8	4.5	-
6.0	-	42.0
6.5	2.3	-
24.0	0.4	16.3
30.5	0.07	15.4

Pt #B

Time (hours)	Blood Plasma (% of adm.)	Total Body (% of adm.)
6.0	20.8	68.0
24.0	7.0	36.0
48.0	4.7	29.0

Pt #A

Time (hours)	Blood Plasma (% of adm.)	Total Body (% of adm.)
3.0	--	69.0
6.0	3.75	55.0
24.0	1.74	55.0
48.0	1.29	49.0

TABLE II

Tc-99m Pyrophosphate Total Body Retention

$$T.B. = A\, e^{-\lambda_1 t} + Be^{-\lambda_2 t}$$
$$Bone = Be^{-\lambda_2 t}$$

	Disease	A	λ_1	B	λ_2
A	Metastatic Carcinoma of Beast (multiple lesion)	0.38	0.693	0.62	0.0050
B	Metastatic Metanoma with ↑ Alkphos	0.56	0.139	0.44	0.0087
C	Benign Prostatic Hypertrophy	0.78	0.231	0.22	0.0108

TABLE III

Cumulative Activity

$$\tilde{A}\ \frac{mCi \cdot hours}{mCi}$$

Patient	Total Body	Bone
A	5.6	5.2
B	6.8	3.6
C	4.0	1.7

TABLE IV

Dose Equivalent for Tc-99m

Rem/μCi • day

Target / Source	Total Body	Skeleton	Testes	Ovaries	Red Marrow
Total Body	4.69×10^{-5}	6.06×10^{-5}	3.98×10^{-5}	5.73×10^{-5}	6.92×10^{-5}
Cortical Bone*	4.83×10^{-5}	2.88×10^{-4}	1.54×10^{-5}	1.69×10^{-5}	9.91×10^{-5}
Cancellous Bone**	4.83×10^{-5}	2.51×10^{-4}	1.54×10^{-5}	1.69×10^{-5}	2.19×10^{-4}

* Assuming Tc-99m in bone is entirely in cortical bone.

** Assuming Tc-99m in bone is entriely in cancellous bone.

TABLE V

Average Radiation Dose Tc-99m Pyrophosphate

(mRem/mCi)

Target / Source		Total Body	Skelton	Testes	Ovaries	Red Marrow
Total Body	A	10.8	14.2	9.3	13.3	16.6
	B	11.2	14.6	9.7	13.8	16.6
	C	7.7	10.0	6.6	6.2	11.4
Cortical Bone	A	10.4	62.4	3.3	3.6	21.4
	B	7.2	43.2	2.3	2.5	14.8
	C	3.4	20.4	1.1	1.0	7.0
Cancellous Bone	A	10.4	52.3	3.3	3.6	47.4
	B	7.2	37.4	2.3	2.5	32.9
	C	3.4	17.7	1.1	1.0	15.5

e. Monitoring of Cs-137 Levels in Man

Almost five years ago we resumed a program started in 1959 by Meneely et al to monitor Cs-137 levels in a population of normal individuals. Last year we measured 8 individuals. The mean value for last year's measurements was found to be 2.9 ± 1.3 nanocuries. Figure 1 shows the comparison of the measurements made to date at Vanderbilt as compared to measurements made at Oak Ridge National Laboratory.

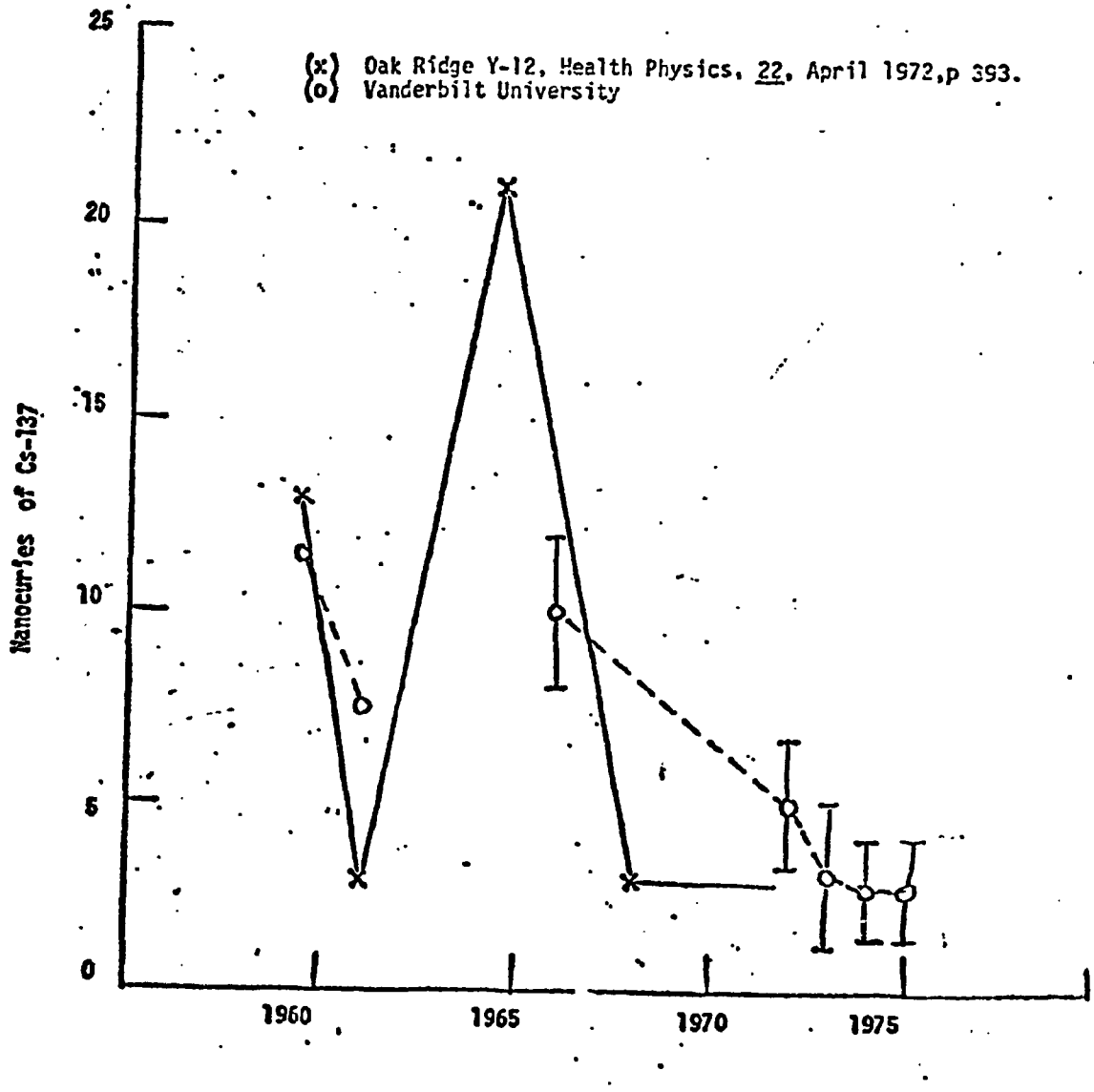

Fig. 1: Body burdens of Cs-137.Whole body counter measurements:

f. Iodine Metabolism and Dosimetry in I-131 Therapy

One year ago the Bureau of Radiological Health supported a study to obtain dosimetry data on patients included in the PHS(BRH)-sponsored cooperative thyrotoxicosis therapy follow-up study. The calculations of the radiation-absorbed dose to the thyroid were carried out by means of non-linear compartmental modelling analysis using the SAAM-25 model shown in Figure 1. The model parameter describing the uptake rate of radioiodine in the thyroid was assumed to be a function of the number of active thyroid cells. The number of cells was, in turn, assumed to be dependent upon the cumulative radiation dose.

Since that time, work on a revised model to accomodate data made available to us by Dr. Brown Dobyns of the Cleveland Memorial General Hospital has been carried out. These new data include measurements on blood levels of MIT, DIT and thyroglobulin (TG) in addition to the measurements of PBI, T3, T4, urine and thyroid activity. The importance is that the kinetics of MIT, DIT, and TG reflect thyroid radiation damage directly and consequently may yield more reliable information on the time course of radiation damage and the degree of biological sensitivity of the thyroid gland.

This work has been described in detail in an appended document entitled "A Model of Iodine Metabolism in a T_3-Thyrotoxic Patient Undergoing I-131 Therapy." The basic conclusions found from this work are as follows.

Iodine metabolism measurements obtained during 4 separate therapies of a T_3-thyrotoxic patient can be represented adequately by a 7-compartment model. Data on radioactivity in various fractionated iodine compounds are simulated well by a non-linear, non-steady-state, dose-dependent model (doses for this study ranged from 9-17 mCi).

Data on four out of thirty two different sets of measurements could not be simulated very well. It is possible that altering some of the simplifying assumptions used in the kinetic model, as discussed in Appendix I, would lead to better fits to these data. Especially, during Treatment 3, metabolism was modified due to administration of PTU and KI but the model is not structured to take such changes into account.

As in the case of a 4-compartment model for iodine metabolism in hyperthyroid patients during I-131 therapy with I-131 activities up to 17 mCi, the 7-compartment model for T_3-thyrotoxicosis therapy also indicates that the apparent volumes of distribution for different iodine compounds do not change appreciably during therapy in this dose range.

Our attempts at compartmental analysis of radioactivity data during I-131 therapy of T_3-thyrotoxicosis showed that independent metabolic routes must be provided for different iodinated compounds secreted by the thyroid, if satisfactory fits were to be attained.

Efforts to establish a reasonable model of the temporal sequence of damage to the thyroid are underway, and hopefully will give information that may be of value to choice of therapy.

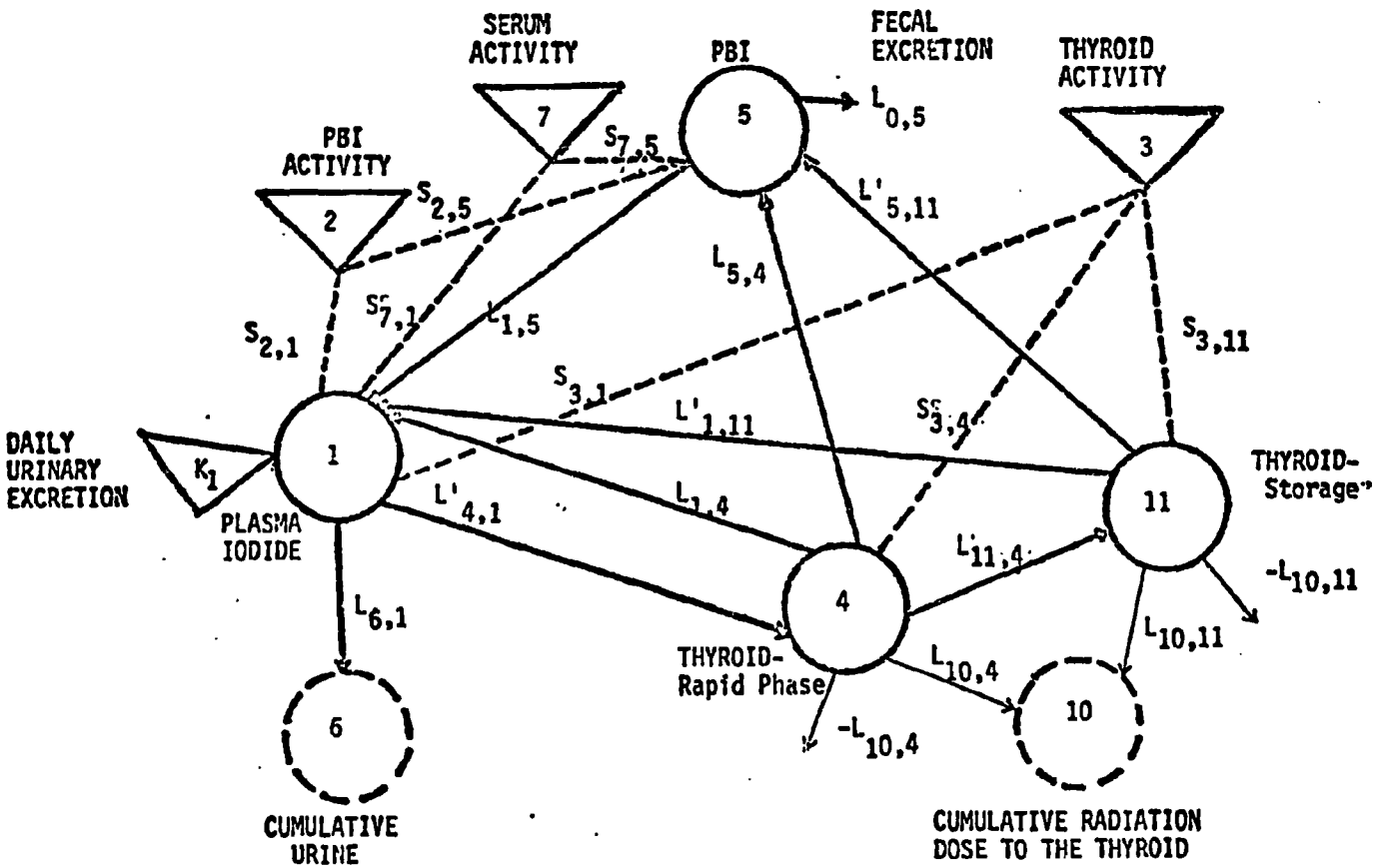

FIG. 1. THE FOUR-COMPARTMENT DOSE-DEPENDENT MODEL.

B. Clinical Applications of Activation Analysis

1. Measurement of Deuterium and Deuterium Labelled Compounds Using the (γ, n) Reaction

Our work on using the (γ, n) reaction with deuterium in stable tracer studies is presently pending availability of suitable radioactive sources. We still feel that either regional facilities using very large ^{24}Na (T-1/2 15 hour) sources or facilities using ^{56}Co (T-1/2 77 days) are feasible. We have discussed with Oak Ridge the possibility of producing large ^{24}Na sources biweekly or monthly for a year to test the utility of a regional deuterium (γ, n) facility but as of yet they have not received the go ahead. Los Alamos has relayed to us that they possibly could produce ^{56}Co for us but we have not been able to procure any yet. ^{88}Y which they will have available shortly will not be useful for deuterium analysis.

2. Cf-252 Neutron Activation Facility - feasiblity study

We have made calculations and done pilot studies investigating the dosimetry associated with two methods of measuring bone mineral content in the forearm using a Cf-252 neutron source. In both methods, the source would be moderated to obtain a beam of thermal neutrons which irradiate a portion of the forearm. One method involves having the patient place his arm first in the neutron beam where Ca-48 will be activated and then between two NaI detectors where the γ-rays given off by Ca-49 are counted. The other method permits both calcium and phosphorous content to be measured by counting the prompt γ-rays given off when neutrons are captured. Two Ge(Li) detectors outside of and facing the beam would be used to count the prompt gammas while the patient's arm is being irradiated. Both techniques could be performed in series, of course, with only one irradiation of the arm, providing data on calcium and phosphorous content. We have carried out a number of calculations designed to estimate the radiation absorbed dose associated with these new procedures.

For thermal neutrons, the dose is given by (1):

$$\text{Dose} = 3.73 \times 10^{-3}\ Ft\ \frac{\text{mRem} - \text{hr}^{-1}\ \text{cm}^2}{\text{neutron} - \text{sec}^{-1}}$$

where F is the neutron flux and t is the irradiation time. The calculations for the Ft values for each of these procedures are given Appendix III. Considering the proposed system geometry, we have estimated that a 10 cm portion of the forearm is irradiated and that 3.5 gm of calcium and 1.7 gm of phosphorous are present (2). To obtain 1000 counts from the activation of calcium, $Ft = 1.5 \times 10^8$ neutrons/cm^2 and the dose to the forearm is ~.2 rem. The dose in the prompt γ analysis would be about 2.0 rem if 1000 counts are to obtained in the phosphorous peak ($Ft = 1.3 \times 10^9$ neutrons/cm^2).

---

[1] D.H. Stoddard and M.E. Hootman, "^{252}Cf Shielding Guide," AEC Report DP-1246.

[2] J.R. Cameron (principal investigator), Progress Report, AEC Contract #AT-(11-1)-1422, 1968.

C. Appendix I

Derivation of analytical time-activity functions from compartmental model rate constants

A. Marrow

Considering the Vanderbilt SAAM-25 iron kinetics model shown below, one can write the equation describing the contents of the marrow compartment M(t).

$$\frac{dm(t)}{dt} = \lambda_1 P(t) - \lambda_2 M(t), \text{ where} \quad (1)$$

P(t) is the contents of the plasma compartment and can be reasonably approximated (for dosimetric purposes) by an exponential function

$$D(t) = Be^{-\lambda pt}, \text{ where} \quad (2)$$

B is the initial amount injected and λp is the effective decay constant and includes loss to stores as to marrow. To a first approximation.

$$\lambda_p = \frac{0.693}{T_{\frac{1}{2}}}, \quad (3)$$

$T_{\frac{1}{2}}$ is the routinely measured plasma diasppearance half-time.

Possibly a better estimate of λp can be derived from the red blood cell (RBC) incorporation curve:

$$\lambda_p = \frac{\lambda_1 B}{R_\tau}, \text{ where} \quad (4)$$

R_τ is the maximum incorporation percentage of radioiron in the circulating RBC, (this derivation can be found in section e).

Substituting the equation of P(t) into equation (1) we have

$$\frac{dm(t)}{dt} = \lambda_1 Be^{-\lambda pt} - \lambda_2 M(t) \quad (5)$$

Rewriting in operator notation,

$$D(m(t) + \lambda_2) = \lambda_1 e^{-\lambda pt}$$

The general solution for this is given by:

$$M(t) = Ce^{-\lambda_2 t} + e^{-\lambda_2 t} \int \lambda_1 Be^{\lambda_2 t} e^{-\lambda pt}\, dt$$

or

$$M(t) = Ce^{-\lambda_2 t} + \frac{\lambda_1 B}{\lambda_2 - \lambda_{pt}} e^{-\lambda pt}$$

Applying the boundary conditions

$$M(t) = 0 \text{ at } t = 0$$

$$C = - \frac{\lambda_1 B}{\lambda_2 - \lambda_p}$$

therefore, $M(t) = \frac{\lambda_1 B}{\lambda_2 - \lambda_p} (e^{-\lambda_p t} - e^{-\lambda_2 t})$ (6)

B. Red Blood Cells

Again, referring to the model below the equation describing the activity in the circulating RBC compartment is:

$$\frac{dR(t)}{dt} = \lambda_2 M(t) \quad (7)$$

Substituting M(t) from equation (6) into (7)

$$\frac{dR(t)}{dt} = \lambda_2 \left[\frac{\lambda_1 B}{\lambda_2 - \lambda_p} (e^{-\lambda_p t} - e^{-\lambda_2 t}) \right] \quad (8)$$

Solving by integration

$$R(t) = - \frac{\lambda_1 \lambda_2 B}{\lambda_p(\lambda_2 - \lambda_p)} e^{-\lambda_p t} + \frac{\lambda_1 B}{\lambda_2 - \lambda_p} e^{-\lambda_2 t} + D$$

Applying boundary conditions

$$R(t) = 0 \text{ at } t = 0$$

$$D = \frac{\lambda_1 B}{\lambda_2 - \lambda_p} \frac{\lambda_2}{\lambda_p} (1 - e^{-\lambda_p t}) + e^{-\lambda_2 t} - 1$$

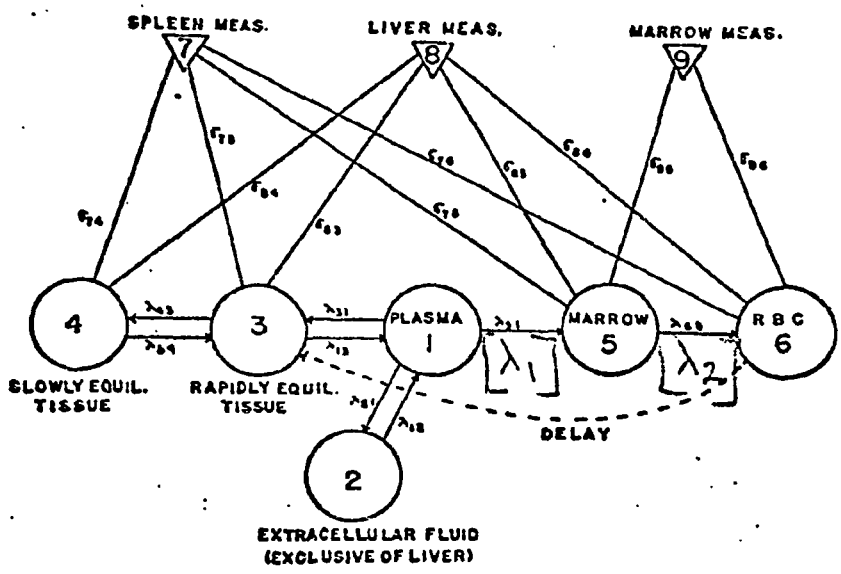

Schematic of SAAM compartmental model for Iron kinetics.

C. Calculation of $\tilde{A}(\tau)$ for Marrow($\tau \to \infty$)

let $F = \dfrac{\lambda_1 B}{\lambda_2 - \lambda p}$ and k = 0.0154/day (λ physical for Fe-59)

$$\tilde{A}m(\tau) = \int_0^\tau F(e^{-\lambda pt} - e^{-\lambda_2 t})\, e^{-kt}\, dt$$

$$= F \int_0^\infty (e^{-(\lambda p + k)} - e^{-(\lambda_2 + k)t}\, dt$$

$$= \frac{\lambda_1 B}{\lambda_2 - \lambda p} \quad \frac{1}{\lambda p + k} - \frac{1}{\lambda_2 + k}$$

$\lambda_p = \dfrac{\lambda_1 B}{R}$, R = Max RBC incorporation

$$\tilde{A}m(\infty) = \frac{\lambda_1 B R\tau}{\lambda_2 R\tau - \lambda_1 B} \left[\frac{R\tau}{\lambda_1 B + 0.0154 R\tau} - \frac{1}{\lambda_2 + 0.0154} \right]$$

D. Calculation of $\tilde{A}(t)$ for RBC ($\tau \to \infty$)

$$\tilde{A}_{RBC} = F \int_0^{\tau} \left(\frac{\lambda_2}{\lambda p} (1 - e^{-\lambda p t}) + e^{-\lambda_2 t} - 1 \right) e^{-kt} \, dt$$

$$= F \int_0^{\infty} \left(\frac{\lambda_2}{\lambda p} e^{-kt} - \frac{\lambda_2}{\lambda p} e^{-(\lambda p + k)t} \right.$$

$$= F \frac{\lambda_2}{\lambda p} \left(\frac{1}{k}\right) - \frac{\lambda_2}{\lambda p} \left(\frac{1}{\lambda p + k}\right) + \left(\frac{1}{\lambda_2 + k}\right) - \frac{1}{k}$$

$$= F \frac{\lambda_2}{\lambda p} \left(\frac{1}{k} - \frac{1}{\lambda p + k}\right) - \left(\frac{1}{k} - \frac{1}{\lambda_2 + k}\right)$$

$$\tilde{A}_{RBC}(\infty) = \frac{\lambda_1 B R\tau}{\lambda_2 R\tau - \lambda_1 B} \quad \frac{\lambda_2 R\tau}{\lambda_1 B} \left(\frac{1}{0.0154} - \frac{R_\tau}{\lambda_1 B + 0.0154 \, R\tau}\right) - \left(\frac{1}{k} - \frac{1}{\lambda_2 + k}\right)$$

E. Derivation of λp from $R(\tau)$

In order to estimate λp one may evaluate $R(t)$ at $t = \tau$ when $\tau \geq 15$ days. At times greater than 15 days $R(\tau)$ should approximately equal R_{max}, the maximum RBC incorporation. Using this assumption we can solve for λp in terms of the λ's and R_{max}.

$$R(\infty) \simeq R_{max} = \left(\frac{\lambda_1 B}{\lambda_2 - \lambda p}\right) \left(\frac{\lambda_2}{\lambda p} - 1\right) = \frac{\lambda_1 B}{\lambda p}$$

$$\lambda p = \frac{\lambda_1 B}{R_{max}}$$

C. Appendix II

Absorbed dose tabulation Fe-59 citrate in abnormals (mrem/μCi)

PATIENT

A

SOURCE / TARGET	RED MARROW	BLOOD	LIVER	SPLEEN	TOTAL
LIVER	.6	23.6	65.9	.5	90.6
SPLEEN	.6	22.8	1.7	150.0	175.1
MARROW	13.5	21.7	1.6	.6	37.4
OVARIES	1.7	22.1	1.4	.3	25.4
TESTES	.2	23.0	.3	.1	23.6
TOTAL BODY	1.1	20.3	3.3	1.1	25.8

B

SOURCE / TARGET	RED MARROW	BLOOD	LIVER	SPLEEN	TOTAL
LIVER	.3	8.1	211.4	2.7	222.5
SPLEEN	.3	7.8	5.5	750.1	763.7
MARROW	8.2	7.4	5.2	2.8	23.6
OVARIES	1.0	7.6	4.4	1.5	14.5
TESTES	.1	7.9	1.0	.3	9.3
TOTAL BODY	.7	7.0	10.7	5.4	23.7

C

SOURCE / TARGET	RED MARROW	BLOOD	LIVER	SPLEEN	TOTAL
LIVER	.2	3.8	252.0	2.7	258.7
SPLEEN	.2	3.6	6.5	750.1	760.4
MARROW	4.3	3.5	6.2	2.8	16.8
OVARIES	.5	3.5	5.3	1.5	10.8
TESTES	.1	3.1	1.2	.3	5.3
TOTAL BODY	.4	3.2	12.7	5.4	21.7

D

SOURCE / TARGET	RED MARROW	BLOOD	LIVER	SPLEEN	TOTAL
LIVER	.6	23.6	105.7	4.6	134.5
SPLEEN	.6	22.8	2.7	1269.4	1295.5
MARROW	13.5	21.7	2.6	4.7	42.5
OVARIES	1.7	22.1	2.2	2.5	28.5
TESTES	.2	23.0	.5	.5	24.2
TOTAL BODY	1.1	20.3	5.3	9.1	35.8

E

SOURCE / TARGET	RED MARROW	BLOOD	LIVER	SPLEEN	TOTAL
LIVER	1.3	18.4	105.7	.5	126.0
SPLEEN	1.3	17.8	2.7	150.0	171.9
MARROW	31.6	16.9	2.6	.6	51.7
OVARIES	3.9	17.2	2.2	.3	23.6
TESTES	.5	17.9	.5	.1	19.0
TOTAL BODY	2.6	15.8	5.3	1.1	24.9

PATIENT

F

SOURCE / TARGET	RED MARROW	BLOOD	LIVER	SPLEEN	TOTAL
LIVER	7•8	2•2	105•7	2•7	118•4
SPLEEN	7•9	2•1	2•7	750•1	762•8
MARROW	184•4	2•8	2•6	2•8	191•8
OVARIES	22•6	2•0	2•2	1•5	28•3
TESTES	2•7	2•1	•5	•3	5•6
TOTAL BODY	15•3	1•9	5•3	5•4	27•9

G

SOURCE / TARGET	RED MARROW	BLOOD	LIVER	SPLEEN	TOTAL
LIVER	•2	2•3	422•8	1•1	426•3
SPLEEN	•2	2•2	10•9	300•0	313•4
MARROW	5•5	2•1	10•4	1•1	19•1
OVARIES	•7	2•1	8•8	•6	12•2
TESTES	•1	2•2	2•1	•1	4•5
TOTAL BODY	•5	1•9	21•3	2•1	25•9

H

SOURCE / TARGET	RED MARROW	BLOOD	LIVER	SPLEEN	TOTAL
LIVER	•1	2•0	158•5	1•0	161•6
SPLEEN	•1	2•0	4•1	265•4	271•6
MARROW	1•0	1•9	3•9	1•0	8•5
OVARIES	•2	1•9	3•3	•5	6•0
TESTES	•0	2•0	•8	•1	2•9
TOTAL BODY	•1	1•8	8•0	1•9	11•8

I

SOURCE / TARGET	RED MARROW	BLOOD	LIVER	SPLEEN	TOTAL
LIVER	•8	14•8	154•5	•6	170•7
SPLEEN	•8	14•3	4•0	161•6	180•7
MARROW	19•5	13•6	3•8	•6	37•5
OVARIES	2•4	13•9	3•2	•3	19•8
TESTES	•3	14•4	•8	•1	15•5
TOTAL BODY	1•6	12•7	7•8	1•2	23•3

J

SOURCE / TARGET	RED MARROW	BLOOD	LIVER	SPLEEN	TOTAL
LIVER	•3	15•8	158•5	•5	175•2
SPLEEN	•3	15•3	4•1	150•0	169•7
MARROW	7•7	14•5	3•9	•6	26•7
OVARIES	•9	14•8	3•3	•3	19•4
TESTES	•1	15•4	•8	•1	16•4
TOTAL BODY	•6	13•6	8•0	1•1	23•3

PATIENT

K

SOURCE / TARGET	RED MARROW	BLOOD	LIVER	SPLEEN	TOTAL
LIVER	.5	.3	333.3	.8	334.9
SPLEEN	.5	.3	8.6	225.0	234.4
MARROW	12.2	.3	8.2	.8	21.5
OVARIES	1.5	.3	7.0	.4	9.2
TESTES	.2	.3	1.6	.1	2.2
TOTAL BODY	1.0	.2	16.8	1.6	19.7

L

SOURCE / TARGET	RED MARROW	BLOOD	LIVER	SPLEEN	TOTAL
LIVER	.6	15.3	158.5	.5	175.0
SPLEEN	.6	14.8	4.1	150.0	169.5
MARROW	13.8	14.1	3.9	.6	32.4
OVARIES	1.7	14.3	3.3	.3	19.6
TESTES	.2	14.9	.8	.1	15.9
TOTAL BODY	1.2	13.2	8.0	1.1	23.4

M

SOURCE / TARGET	RED MARROW	BLOOD	LIVER	SPLEEN	TOTAL
LIVER	.4	7.4	105.7	1.1	114.6
SPLEEN	.4	7.2	2.7	300.0	310.4
MARROW	9.1	6.8	2.6	1.1	19.7
OVARIES	1.1	7.0	2.2	.6	10.9
TESTES	.1	7.2	.5	.1	8.0
TOTAL BODY	.8	6.4	5.3	2.1	14.6

N

SOURCE / TARGET	RED MARROW	BLOOD	LIVER	SPLEEN	TOTAL
LIVER	.4	10.2	131.7	.8	143.1
SPLEEN	.4	9.8	3.4	225.0	238.7
MARROW	9.7	9.3	3.2	.8	23.1
OVARIES	1.2	9.5	2.8	.4	13.9
TESTES	.1	9.9	.6	.1	10.8
TOTAL BODY	.8	8.7	6.6	1.6	17.8

O

SOURCE / TARGET	RED MARROW	BLOOD	LIVER	SPLEEN	TOTAL
LIVER	.2	1.0	333.3	1.1	335.6
SPLEEN	.2	1.0	8.6	300.0	309.8
MARROW	4.3	.9	8.2	1.1	14.5
OVARIES	.5	.9	7.0	.6	9.0
TESTES	.1	1.0	1.6	.1	2.8
TOTAL BODY	.4	.9	16.8	2.1	20.2

PATIENT

P

SOURCE / TARGET	RED MARROW	BLOOD	LIVER	SPLEEN	TOTAL
LIVER	1•1	4•5	211•4	•8	217•9
SPLEEN	1•1	4•4	5•5	225•0	236•0
MARROW	26•1	4•2	5•2	•8	36•3
OVARIES	3•2	4•3	4•4	•4	12•3
TESTES	•4	4•4	1•0	•1	5•9
TOTAL BODY	2•2	3•9	10•7	1•6	18•3

Q
(NORMAL)

SOURCE / TARGET	RED MARROW	BLOOD	LIVER	SPLEEN	TOTAL
LIVER	•7	23•2	52•8	•5	77•4
SPLEEN	•7	22•5	1•4	150•0	174•6
MARROW	17•3	21•4	1•3	•6	40•6
OVARIES	2•1	21•0	1•1	•3	25•3
TESTES	•3	22•6	•3	•1	23•2
TOTAL BODY	1•4	20•0	2•7	1•1	25•2

C. Appendix III: Calculations for Neutron Fluence.

Calculations for neutron fluence are shown in this appendix for neutron activation of calcium in the forearm and prompt analysis of calcium and phosphorous in the forearm.

1. Neutron Activation Analysis

If a mass, m, is activated for a time t in a neutron flux, F, and then placed in front of a detector, the number of counts obtained is given

$$C = \frac{\sigma_c N_A A_I I_\gamma E_\gamma \ (1 - e^{-\lambda t}) \ (e^{-\lambda t_1} - e^{-\lambda t_2})}{\lambda A}$$

where $_c$ = thermal neutron capture cross section

N_A = Avogadro's number

A_I = abundance of the isotope

I = intensity of the -ray being counted

E = efficiency of the detector at the -energy

= $\ln 2/T_{\frac{1}{2}}$ ($T_{\frac{1}{2}}$ = half life of activated isotope

t_1 = time after irradiation that the count is begun

t_2 = time after irradiation that the count is ended

and A = atomic weight of element.

For short irradiation times (with respect to the half life of the activated isotope)

$$\frac{1 - e^{-\ t}}{\lambda} \approx t$$

then

$$Ft = \frac{CA}{{}_{o_c} N_A M A_I I_\gamma E_\gamma (e^{-\lambda t_1} - e^{-\lambda t_2})}$$

For the activation of Ca-48, σ_c = 1.1 barns,

A_I = .00185, I = .89, $T_{\frac{1}{2}}$ = 8.8 min and A = 40.08. If m = 3.5 gms,

t_1 = 1 minute, t_2 = 20 minutes, E = .10, and C = 1000 counts,

$Ft = 1.5 \times 10^8 \ \frac{\text{neutrons}}{\text{cm}^2}$

2. Prompt Analysis

If a mass, m is placed in a neutron flux, F, for a time, t, while the prompt γ-rays are counted, the number of counts in a photopeak is given by

$$C = \frac{\sigma_c M N_A I_\gamma E_\gamma t F}{A}$$

where the terms are defined as before. For the 6.42 MeV peak from calcium (1), σ_c = .43 barns and I = .2809. If the detector efficiency is E = 7 x 10^{-4} and C = 1000, then,

$$Ft = 2.2 \times 10^8 \frac{n}{cm^2}$$

For the 3.90 MeV peak from phosphorous (1), A = 30.974 σ_c = .19 barns and I = .1758. To obtain 1000 counts with 1.7 gms present, Ft = 1.3 x 10^9 neutrons/cm^2.

---

[1] D. Duffey, A. El-Kady and F.E. Seuftle, "Analytical Sensitivities and Energies of Thermal-Neutron-Capture Gamma Rays," Nucl Inst and Methods 80 (1970), 149.